UNIVERSITY OF OKLAHOMA

GRADUATE COLLEGE

DESIGN AND REALIZATION OF A TUNABLE MICROSTRIP BANDSTOP FILTER BASED ON CHARACTERISTIC-POLYNOMIAL TRANSFORMATION

A THESIS

SUBMITTED TO THE GRADUATE FACULTY

in partial fulfillment of the requirements for the

Degree of

MASTER OF SCIENCE

By

SAMUEL ANTONIO ESPINOZA FLORES
Norman, Oklahoma
2026

DESIGN AND REALIZATION OF A TUNABLE MICROSTRIP BANDSTOP FILTER BASED ON CHARACTERISTIC-POLYNOMIAL TRANSFORMATION

A THESIS APPROVED FOR THE
SCHOOL OF ELECTRICAL AND COMPUTER ENGINEERING

BY THE COMMITTEE CONSISTING OF

Dr. Hjalti Sigmarsson, Chair

Dr. Russell Kenney

Dr. Choon Yik Tang

Acknowledgments

I would like to express my deepest gratitude to my advisor, Dr. Hjalti Sigmarsson, for his constant support, guidance, and mentorship throughout the past two years. His patience, encouragement, and constant willingness to share his knowledge were essential to the completion of this work. I am especially grateful for the time, effort, and confidence he invested in me during every stage of this research. Without his guidance and dedication, this work would not have been possible.

I would also like to sincerely thank my wife for standing by my side during the most stressful moments and for always motivating me to pursue higher goals. Her encouragement, understanding, and support gave me strength throughout this journey.

Finally, I am deeply grateful to the rest of my family for their constant belief in me, their unconditional support, and for always being there whenever I needed them.

Table of Contents

List of Figures

List of Tables

Abstract

Rapid advances in communication systems have increased the demand for efficient spectral allocation and interference mitigation techniques. Among the available solutions, frequency-agile filters are especially attractive because they allow the tuning of key response characteristics such as center frequency and filter shape. Although substantial research has been dedicated to tunable filters, achieving a comprehensive and practical design remains challenging due to limitations in complexity, implementation, and physical size.

Multiple tuning mechanisms have been reported for tunable filters, with mechanical and electronic tuning being among the most common. Electronic tuning can be realized through elements such as p-i-n diodes, varactor diodes, and radio-frequency (RF) microelectromechanical systems (MEMS) switches. These devices can be integrated into microstrip structures, making microstrip technology a practical platform for the implementation of reconfigurable filters.

In this regard, tunable bandstop filters with rejection bandwidths broader than those of conventional notch responses remain less commonly reported than their bandpass counterparts, particularly when a synthesis-based design approach is pursued. This makes their study especially relevant for applications requiring increased rejection bandwidth along with tunability. In this work, a narrowband bandstop filter with an enhanced rejection bandwidth is developed from the theoretical foundation of polynomial synthesis. It is shown that by switching the numerators of the character-

istic polynomials, a bandstop response can be obtained from an equi-ripple bandpass prototype, resulting in a broader rejection band than that of a typical notch bandstop filter.

Chapter 1

Introduction and Background

1.1 Overview

In the field of communication systems, rapid advancements in RF front-end architectures have significantly increased the demand for efficient and adaptable spectral allocation. Multiple methods have been proposed to address the limitations of the electromagnetic spectrum, including frequency-agile filtering [1, 2].

In general terms, a microwave filter is a component of the RF front end whose primary function is to select a specific range of frequencies while rejecting out-of-band signals. This frequency selectivity directly influences the overall performance of front-end devices, particularly in terms of signal integrity and interference suppression. Moreover, frequency-agile filters provide tunability that enables real-time spectral selectivity. This adaptability reduces the need for different fixed-frequency filters, leading to lower cost, physical size compactness, and greater flexibility to meet the system requirements. Fig. 1.1 illustrates a tunable bandstop filter operating at different center frequencies, along with the corresponding rejection response.

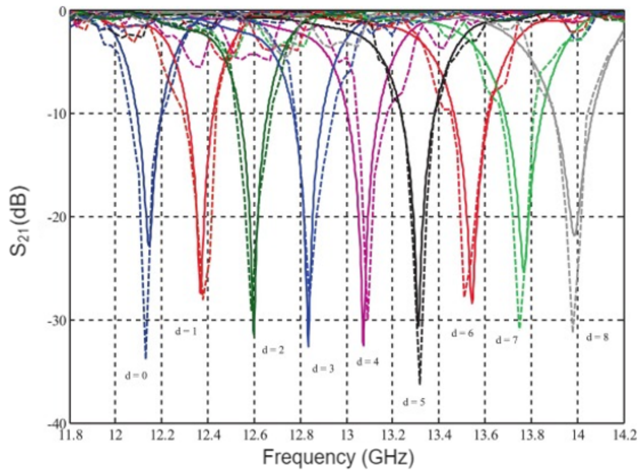

Figure 1.1: Tunable bandstop filter rejection. Adapted from [3]

Tunable filters can be realized through several tuning approaches, such as mechanical, optical, thermal, and electronic methods [1]. Among these, electronic tuning is one of the most widely adopted because it enables compact implementation and relatively fast adjustment of the filter response. In practice, this approach is commonly achieved using components such as p-i-n diodes, varactor diodes, and RF microelectromechanical systems (MEMS) switches.

Nevertheless, each of these devices introduces certain limitations that must be considered during the design stage. Varactor diodes, for example, often suffer from limited linearity, whereas p-i-n diodes generally require higher power consumption. In addition, both technologies depend on external biasing networks, which increase design complexity and pose a challenge in their integration into microstrip filter structures. For this reason, the selection of the tuning element is not only a matter of achieving tunability, but also of balancing electrical performance, biasing requirements, and fabrication practicality.

1.2 Motivation

Although significant research has been devoted to improving individual tuning characteristics, particularly the achievement of a wider tuning range, the development of bandstop filters that simultaneously provide high performance, compact size, and seamless integration remains a significant challenge. As reported in [4, 5, 6], several approaches have been proposed to realize tunable bandpass-to-bandstop filters using conventional frequency transformations. However, in many of these designs, the resulting bandstop response exhibits a much narrower rejection bandwidth than the corresponding bandpass response, as illustrated in Fig. 1.2.

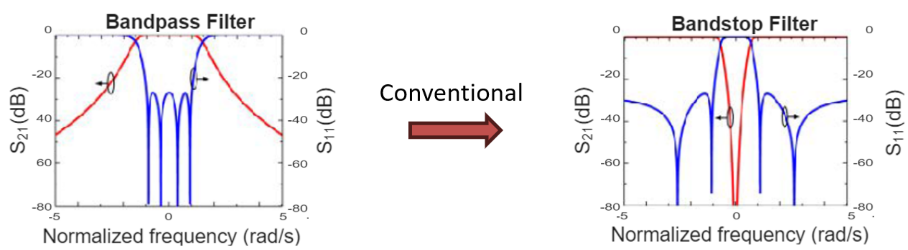

Figure 1.2: Bandpass-to-bandstop transformation using conventional lowpass prototype frequency transformation. Adapted from [7]

To address this limitation, the approach adopted in this work begins with the synthesis of a bandpass prototype. Once this prototype is obtained, the characteristic polynomials are interchanged to generate the corresponding bandstop characteristic. In this way, the bandstop filter preserves the general form of the original bandpass characteristic, but with the transmission and reflection functions effectively exchanged. As a result, the stopband is wider than the narrow rejection typically associated with a conventional notch filter, providing improved interference suppression and greater spectral flexibility, as shown in Fig. 1.3.

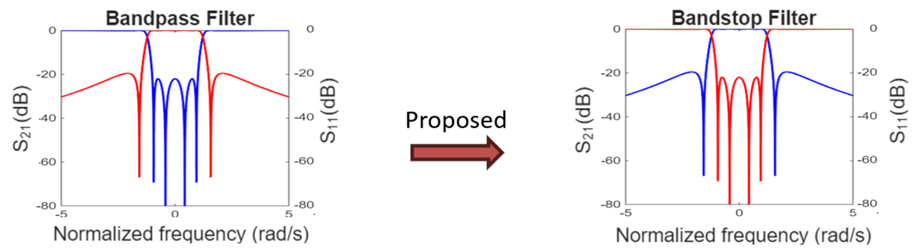

Figure 1.3: Bandpass-to-bandstop transformation using characteristic-polynomial transformation

The proposed design is based on the theoretical framework of polynomial synthesis, which constitutes a fundamental concept in classical filter theory. This approach demonstrates that a bandstop response can be derived directly from a bandpass prototype by modifying the numerators of the characteristic polynomials [7]. This formulation not only provides the basis for the proposed transformation, but also establishes a point of comparison between the bandpass and bandstop structures, making it possible to identify and analyze their main response characteristics.

Finally, planar microstrip filters provide a practical and seamless platform for validating the hypotheses developed in this work. Their compatibility with standard printed-circuit fabrication techniques, along with their widespread use in microwave systems, makes them an appropriate vehicle for translating theoretical concepts into physical implementations.

For this reason, this work not only seeks to demonstrate the proposed bandpass-to-bandstop transformation in a realizable microstrip structure, but also to provide a simple guide to some of the fundamental concepts of microwave filter theory that may support future developments and implementations. The main goal of this work is to demonstrate a streamlined design procedure for tunable bandstop filters based on characteristic-polynomial transformation, providing a practical path from theoretical synthesis to microstrip implementation.

1.3 Literature Review

1.3.1 Planar Microwave Filters

Planar microwave filters emerged during the 1950s with the increasing adoption of printed circuit technology and the rapid growth of microwave engineering. Although early progress was mainly driven by aerospace and military needs, later expansion into telecommunications and consumer applications increased the demand for solutions focused on reducing cost, simplifying fabrication, and enabling mass production. [8].

In microwave engineering, it is common to distinguish between lumped and distributed elements according to their physical dimensions relative to the wavelength of operation. When the dimensions of a circuit element are much smaller than the shortest wavelength of interest, the element can be treated as lumped. In contrast, when the physical dimensions are comparable to the wavelength, the element must be treated as distributed.

This distinction is fundamental because conventional circuit relations, such as Kirchhoff's voltage and current laws, are not directly applicable to distributed structures. Instead, the voltage and current vary with position along the structure, and the electromagnetic behavior must be analyzed using transmission-line theory. For this reason, planar microwave filters are commonly described through equivalent distributed models that capture their electrical behavior more accurately.

Multiple transmission-line structures can be found in microwave filter design, such as microstrip lines, coplanar waveguides, and slotlines. Among these, microstrip technology is especially attractive because of its simple geometry, low fabrication cost, compact size, and easy integration with other microwave and electronic components. For this reason, microstrip filters are of particular interest in this work.

1.3.2 Microstrip Structure

Microstrip is one of the most widely used planar transmission-line structures in microwave filter design because it offers a good balance between compactness, seamless fabrication, and relevance in high-frequency applications. As illustrated in Fig. 1.4, a microstrip line consists of a conducting strip of width W and thickness t printed on the top surface of a dielectric substrate of thickness h and relative permittivity ϵ_r, while the bottom surface of the substrate is completely covered by a ground plane. [9].

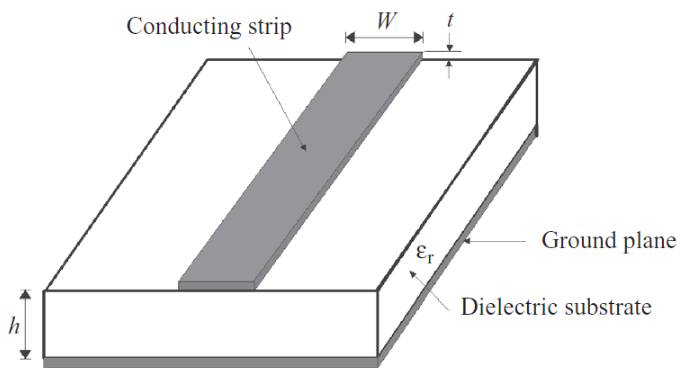

Figure 1.4: General Microstrip Structure. Reproduced from [9]

A microstrip line is considered an inhomogeneous transmission structure because its electromagnetic fields propagate through both the dielectric substrate and the surrounding air. For this reason, it does not support a pure TEM mode. Instead, propagation occurs in a quasi-TEM mode, where the longitudinal field components are much smaller than the transverse ones and are usually neglected in practice. This approximation is important because it enables the analysis of microstrip lines with standard transmission-line theory while still obtaining accurate results over a wide range of frequencies. Under this assumption, several important transmission-line parameters can be determined using the closed-form expressions reported in [9].

The first parameter in microstrip analysis is the guided wavelength λ_g, which represents the wavelength of propagation along the transmission line. Since the fields are shared between air and dielectric, the wave propagation is characterized by an effective dielectric constant ϵ_{eff} rather than the substrate dielectric constant alone. Following [9], the guided wavelength is given by

$$\lambda_g = \frac{\lambda_0}{\sqrt{\epsilon_{eff}}} \tag{1.1}$$

where λ_0 is the free space wavelength. For a microstrip line, the effective dielectric constant ϵ_{eff} can be approximated as [9]

$$\epsilon_{eff} = \frac{\epsilon_r + 1}{2} + \frac{\epsilon_r - 1}{2} \frac{1}{\sqrt{1 + 12h/W}} \tag{1.2}$$

where ϵ_r is the substrate relative dielectric constant, h is the substrate thickness, and W is the strip width.

Another fundamental quantity is the characteristic impedance Z_0, which describes the relationship between voltage and current for a wave propagating along the transmission line. In microstrip structures, Z_0 depends on the geometry of the strip and the electrical properties of the substrate. Also, the phase constant β expressed in (1.3) defines the phase variation of the signal per unit length. Using the phase constant, the electrical length θ of a microstrip section of physical length l can then be written as shown in [9]

$$\beta = \frac{2\pi}{\lambda_g} \tag{1.3}$$

$$\theta = \beta l \tag{1.4}$$

These relations are particularly important in microwave filter design because resonant behavior and coupling conditions are usually defined in terms of electrical length rather than physical length. For example, a transmission-line section shown in Fig. 1.5 has an electrical length of $\pi/2$ when $l = \lambda_g/4$ and π when $l = \lambda_g/2$, with a characteristic impedance represented by $1/Y_a$ [9]. Consequently, the physical dimensions of a microstrip filter must always be interpreted with respect to the guided wavelength at the operating frequency. This provides the link between the theoretical filter parameters and their physical realization.

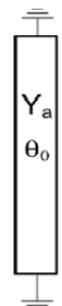

Figure 1.5: Microstrip $\lambda/2$ transmission line. Adapted from [9]

1.3.3 Fundamental Elements of Microstrip Filters

Microstrip filters can be implemented using different types of circuit elements, selected according to the desired response, frequency range, and fabrication limitations. In general, these elements can be broadly classified as lumped elements, quasi-lumped elements, and resonators [9].

Lumped inductors and capacitors are components whose physical dimensions are much smaller than the free-space wavelength at the highest operating frequency, commonly satisfying the condition that their size is less than about $0.1\lambda_0$. Because of their small size, low cost, and ease of use, they are attractive for compact circuits. However, at microwave frequencies they generally exhibit lower quality factor, limited power handling capability, and stronger parasitic effects than distributed implementations.

Quasi-lumped elements are realized using short transmission-line sections that approximate lumped reactances over a narrow frequency range. Typical examples include short high-impedance or low-impedance lines, as well as open-circuited or short-circuited stubs whose physical length is typically much smaller than a $\lambda_g/4$. These elements are especially useful in planar implementations because they can be fabricated directly on the substrate without the need for discrete components.

Among these element types, resonators are the most important in microwave filter design, since they provide a frequency-selective behavior. In general, a resonator stores electric and magnetic energy, which can be represented by capacitance and inductance elements respectively, as illustrated in Fig. 1.6. Moreover, it exhibits resonance at one or more natural frequencies, with the dominant response occurring at the fundamental resonant frequency f_0. In planar filter structures, the resonators establish the passband or stopband characteristics, while the coupling between them determines the bandwidth and shapes the overall response.

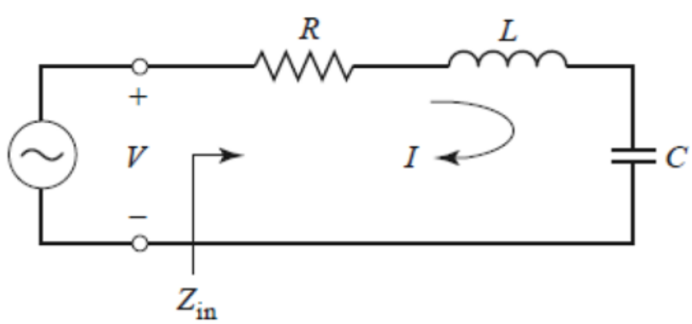

Figure 1.6: Series representation of a single resonator. Adapted from [9]

For this reason, resonators constitute the fundamental building blocks of the filter structures developed in this work. Their resonant behavior, together with the coupling established between adjacent resonators, governs the frequency-selective response of the overall circuit. Accordingly, the following chapters focus on resonator theory and on the physical characteristics that determine their implementation in planar microstrip technology.

1.4 Thesis Outline

This work presents a complete procedure for validating the theoretical analysis of a tunable bandstop filter, beginning with filter synthesis and continuing through physical design, fabrication, and experimental evaluation. The overall workflow is intended to provide a clear connection between the synthesis of the filter and its practical realization in microstrip technology.

Chapter 2 introduces the theoretical framework used for filter synthesis based on characteristic polynomials. The transmission, reflection, and denominator polynomials are described, along with the mathematical techniques used to obtain them, including the recursive technique and the alternating poles method. Once these polynomials are determined, they are used to construct the coupling matrix, which provides a compact representation of the desired filter behavior through its matrix coefficients. These coefficients then serve as the reference for the later physical implementation of the filter.

Chapter 3 moves from synthesis to physical interpretation by focusing on resonators as the fundamental building blocks of the proposed microstrip filter. Their main properties are examined, including resonant behavior, coupling mechanisms, and their relationship to the coupling matrix representation. A single-resonator analysis is then presented to introduce the tunable characteristic responsible for frequency adjustment. The chapter concludes with time-domain tuning analysis, which is used as a practical tool to refine the filter response during full-wave electromagnetic simulation.

Chapter 4 addresses the practical aspects required for fabrication and experimental validation. Particular attention is given to the integration of the DC biasing circuit needed to realize tunability in the microstrip structure. To verify the proposed concept in a progressive manner, a single resonator is first fabricated and measured. After this initial validation, the complete bandstop filter is fabricated and experimentally characterized. The measured results are then analyzed in light of the theoretical and simulated predictions, with discussion of important practical factors such as fabrication tolerances, losses, and implementation constraints.

Finally, Chapter 5 presents the main conclusions of this work and outlines possible directions for future research. It also summarizes the key takeaways from the development of this project, with the intention of providing useful guidance for future implementations of tunable microstrip filters.

Chapter 2

Filter Synthesis and Coupling Matrix

This chapter builds on the advanced synthesis techniques presented in [10]. It introduces a method that explores the fundamental relationships among the scattering parameters, which are used in the polynomial representation of the transmission and reflection characteristics of prototype filtering functions. A MATLAB code was developed to determine the characteristic polynomials $P(s)$, $F(s)$ and $E(s)$, as well as the ripple and normalization coefficient. Moreover, the recursion technique and alternating poles method are used to generate some of these polynomials for Chebyshev filter synthesis. Using these characteristic polynomials, a coupling matrix is then constructed to represent the coupling relationships within the filter and to illustrate how the corresponding coefficients interact. Finally, the resulting scattering parameters are presented in graphical form to show the frequency response of the synthesized network.

2.1 Polynomial Synthesis for Chebyshev Bandpass Filters

In RF and microwave filter implementations, scattering parameters are used to characterize the behavior of electromagnetic waves in terms of incident and reflected power at each port of a network, as illustrated in Fig 2.1. At microwave frequencies, direct evaluation of voltages and currents along the structure becomes impractical due to their frequency-dependent nature. Consequently, scattering parameters provide a more convenient framework for network analysis.

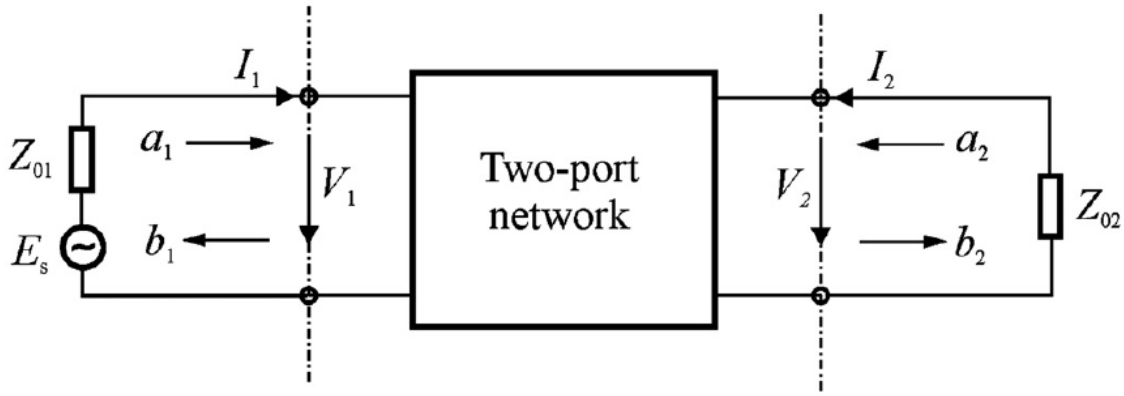

Figure 2.1: Two-port network. Reproduced from [9]

The scattering matrix shown in (2.1) represents the relationship between incident waves (a_1,a_2) and reflected waves (b_1,b_2), which characterizes the input and output behavior of a two-port network through the parameters S_{11}, S_{12}, S_{21}, and S_{22}.

$$\begin{bmatrix} b_1 \\ b_2 \end{bmatrix} = \begin{bmatrix} S_{11} & S_{12} \\ S_{21} & S_{22} \end{bmatrix} \cdot \begin{bmatrix} a_1 \\ a_2 \end{bmatrix} \tag{2.1}$$

For a passive, lossless, and reciprocal network, the scattering matrix must satisfy energy conservation and orthogonality conditions. The first instance requires that the total power at each port is preserved, meaning that the sum of the transmitted and reflected power is equal to unity (2.2), (2.3). The second attribute defines the cross-products of the transmission and reflection coefficients must satisfy orthogonality (2.4). These properties ensure that the total power is conserved and the network exhibits reciprocal behavior.

$$S_{11}(s)S_{11}(s)^* + S_{21}(s)S_{21}(s)^* = 1 \tag{2.2}$$

$$S_{22}(s)S_{22}(s)^* + S_{12}(s)S_{12}(s)^* = 1 \tag{2.3}$$

$$S_{11}(s)S_{12}(s)^* + S_{21}(s)S_{22}(s)^* = 0 \tag{2.4}$$

The synthesis of Chebyshev bandpass filters is based on the formulation of characteristic polynomials that define the transmission and reflection responses of the network. In particular, three polynomials are of primary importance: transmission polynomial $P(s)$, reflection polynomial $F(s)$, and denominator polynomial $E(s)$. These polynomials describe the filtering function and establish the foundation for subsequent coupling matrix synthesis.

The mathematical structure and generation of these polynomials follow the methodology presented in the literature [10]. This procedure provides a systematic approach to derive the filtering function, which is subsequently used to obtain the coupling matrix representation of the filter. The following subsections describe in detail the definition, properties, and synthesis of each characteristic polynomial.

2.1.1 Transmission Polynomial $P(s)$

The transmission polynomial $P(s)$ defines the numerator of the transmission coefficient $S_{21}(s)$, which represents the transfer response of the filter. From this relationship, it follows that $P(s)$ directly controls the selectivity of the filter by determining the location of the transmission zeros, as observed in Fig. 2.2. These transmission zeros correspond to frequencies at which the transmission is ideally zero, resulting in infinite attenuation in the response.

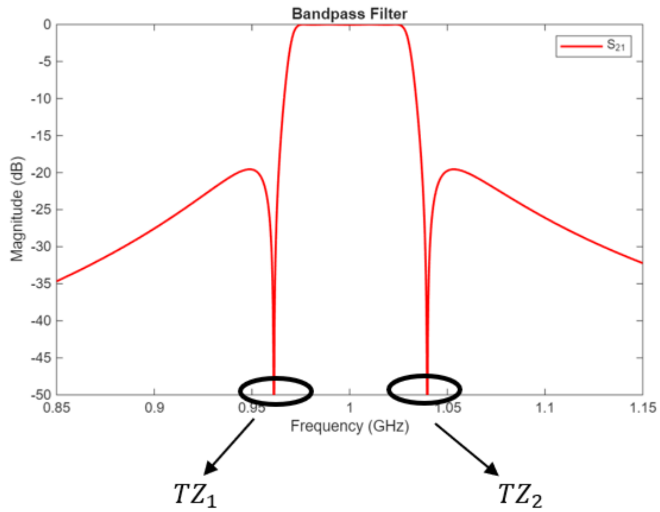

Figure 2.2: Transmission response of a bandpass prototype

The general expression for the transmission coefficient shown in (2.5) represents the proportional relationship between $S_{21}(s)$ and $P(s)$ along with inversely proportion to the common denominator polynomial $E(s)$. Therefore, the roots of $P(s)$ define the frequencies where the transmission is suppressed. The ripple coefficient ϵ serves as a scaling factor to control the passband ripple level, its calculation will be explored later in this chapter.

$$S_{21}(s) = \frac{P(s)/\epsilon}{E(s)} \tag{2.5}$$

Mathematically, the transmission polynomial is expressed as a product of its roots in the frequency domain, where ω is the real frequency variable related to the complex frequency $s = j\omega$. The degree of $P(s)$, denoted as n_{fz}, corresponds to the number of transmission zeros in the filtering function. This expression can be observed in 2.6.

$$P(\omega) = \prod_{n=1}^{n_{fz}} (\omega - \omega_n) \tag{2.6}$$

If the number of transmission zeros is less than the degree N of the denominator polynomial $E(s)$, the remaining transmission zeros are located at infinity. In this case, the transfer function approaches zero as $s \to j\infty$. Two important cases derive from this definition. The first one is when $n_{fz} = 0$, the filter exhibits an all-pole response without finite transmission zeros. The second case is when $0 < n_{fz} < N$, hence the number of transmission zeros at infinity is calculated as $N - n_{fz}$.

The location of the finite transmission zeros depends on the filter specifications and can lie on the real axis, the imaginary, or occur as complex-conjugate pairs. To ensure that the overall filtering function satisfies the required orthogonality conditions, the transmission polynomial must be multiplied by the imaginary unit j. This adjustment depends on the parity of both the filter order N and the total transmission zeros n_{fz}, as summarized in Table 2.1.

Table 2.1: Multiplication of $P(s)$ by j to satisfy the orthogonality condition. Adapted from [10]

N	n_{fz}	$(N - n_{fz})$	Multiply $P(s)$ by j
Odd	Odd	Even	Yes
Odd	Even	Odd	No
Even	Odd	Odd	No
Even	Even	Even	Yes

2.1.2 Reflection Polynomial $F(s)$

The reflection polynomial $F(s)$ determines the numerator of the reflection coefficient $S_{11}(s)$, which characterizes how much of the incident signal is reflected back toward the source instead of being transmitted through the filter. Therefore, $F(s)$ directly governs the reflection response of the network and represents the return loss performance in the passband and the corresponding reflection zeros, as illustrated in

Fig. 2.3. For Chebyshev and Butterworth prototypes, $F(s)$ is an N-degree polynomial with generally complex coefficients.

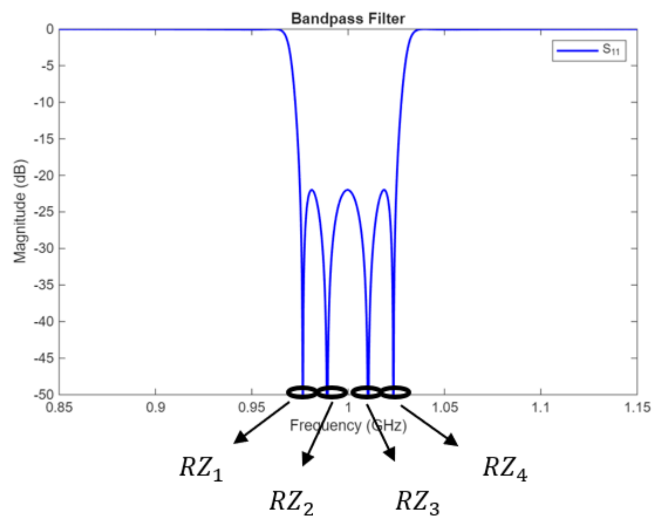

Figure 2.3: Reflection response of a bandpass prototype

The relationship between the reflection coefficient and the characteristic polynomials is given below, where $E(s)$ is the common denominator polynomial and ϵ_R is a normalization constant associated with the specified return loss.

$$S_{11}(s) = \frac{F(s)/\epsilon_R}{E(s)} \tag{2.7}$$

This expression highlights that the roots of $F(s)$ define the frequencies at which the reflection response is minimized or controlled.

The coefficients of $F(s)$ are derived from the filtering function $C_N(\omega)$, which is an N-th degree function whose poles and zeros correspond to the roots of $P(\omega)$ and $F(\omega)$ respectively. This relationship is denoted in [10] as

$$kC_N(\omega) = \frac{F(\omega)}{P(\omega)} \tag{2.8}$$

Here, k is an normalization constant introduced to ensure consistency between the polynomial forms. Particularly, $P(\omega)$ and $F(\omega)$ are defined as monic polynomials, in other words, its highest-degree coefficient is unitary, whereas $C_N(\omega)$ may not have a unity leading coefficient.

The reflection polynomial can be constructed from the numerator of the filtering function, which is defined as the average of two auxiliary functions.

$$F(\omega) = \frac{1}{2}[G_N(\omega) + G'_N(\omega)] \tag{2.9}$$

The functions $G_N(\omega)$ and $G'_N(\omega)$ are expressed as products involving the terms c_n and d_n as shown in (2.10). Here, the variables c_n, d_n are defined as functions of the frequency variable ω and the prescribed transmission zeros ω_n. These terms incorporate both the finite transmission zeros and those located at infinity, guaranteeing a complete representation of the filtering function.

$$G_N(\omega) = \prod_{n=1}^{N}[c_n + d_n], \quad G'_N(\omega) = \prod_{n=1}^{N}[c_n - d_n] \tag{2.10}$$

$$c_n = (\omega - 1/\omega_n) \tag{2.11}$$

$$d_n = \omega' \sqrt{(1 - 1/\omega_n^2)} \tag{2.12}$$

$$\omega' = \sqrt{(\omega^2 - 1)} \tag{2.13}$$

The method to find the coefficients of $F(\omega)$ is called the “recursive technique” [10]. This method constructs the polynomial iteratively, where the n-th order polynomial is obtained from the $(n-1)$-th order result. Therefore, a total of $N-1$ recursive steps are required to obtain the final N-th degree polynomial.

The function $G_N(\omega)$ can then be decomposed into two components $U_N(\omega)$ and

$V_N(\omega)$.

$$G_N(\omega) = U_N(\omega) + V_N(\omega) \tag{2.14}$$

These two polynomials can be represented as the sum of its coefficients shown below [10]:

$$U_N(\omega) = u_0 + u_1\omega + u_2\omega^2 + \cdots + u_N\omega^N \tag{2.15}$$

$$V_N(\omega) = \omega' \left(v_0 + v_1\omega + v_2\omega^2 + \cdots + v_N\omega^N\right) \tag{2.16}$$

Since $G'_N(\omega)$ is the conjugate counterpart of $G_N(\omega)$, it follows that the reflection polynomial $F(\omega)$ is given by the polynomial $U_N(\omega)$.

The resulting polynomial must then be normalized such that its highest-order coefficient is unity. Finally, by applying the transformation from the frequency domain to the complex domain ($s = j\omega$), the reflection polynomial is obtained as $F(s)$. The recursive formulation is implemented in MATLAB, as described in Appendix A.1. In general form, the recursive relationship can be expressed as follows:

$$G_k(\omega) = U_k(\omega) + \omega' V_k(\omega) \tag{2.17}$$

$$G_k(\omega) = G_{k-1}(\omega)\left[(\omega - 1/\omega_k) + \omega'\sqrt{1 - 1/\omega_k^2}\right]$$

This recursive approach provides a systematic and efficient method for constructing the reflection polynomial required for filter synthesis.

2.1.3 Denominator Polynomial $E(s)$

The last characteristic polynomial $E(s)$ plays a central role in the formulation of the scattering parameters. This polynomial is required to be Hurwitz, meaning that all its roots lie in the left half of the complex plane. This condition guarantees the stability and physical realizability of the filter network. In addition, $E(s)$ serves as a common ground for both $S_{11}(s)$ and $S_{21}(s)$, connecting the transmission and reflection responses into a unified mathematical framework. It has an N-th degree, corresponding directly to the order of the filter.

Once the transmission polynomial $P(s)$ and reflection polynomial $F(s)$ have been determined, the denominator polynomial can be obtained using the "alternating pole method", which consists in selecting only the roots on the left side of the complex plane, as shown in Fig. 2.4. This method is derived from the conservation of energy expression shown in (2.2), where the sum of transmitted and reflected power must remain constant. Hence, combining this principle with the fundamental relationship between the characteristic polynomials, the basis for the synthesis procedure can be established. The resulting expression is shown below [10].

$$F(s)F(s)^*/\epsilon_R^2 + P(s)P(s)^*/\epsilon^2 = E(s)E(s)^* \tag{2.18}$$

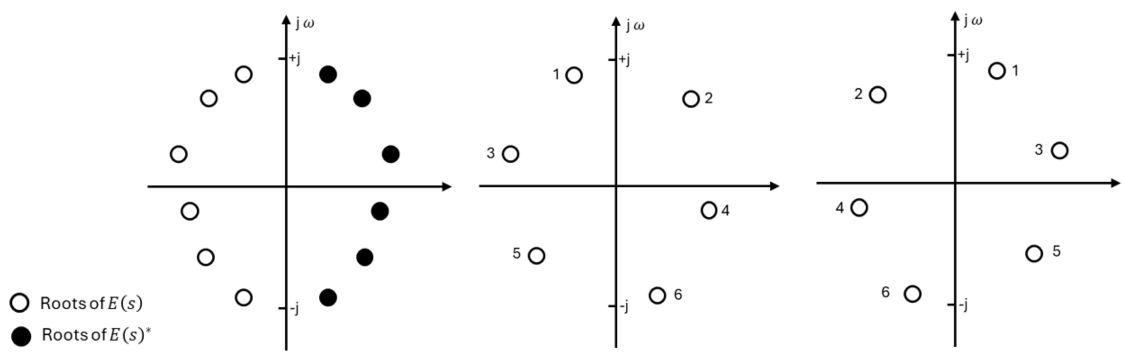

Figure 2.4: Pattern of the roots of: (a) $E(s)E(s)^*$, (b) $[\epsilon_r(jP(s)) + \epsilon F(s)]$, (c) $[\epsilon_r(jP(s)) + \epsilon F(s)]^*$. Adapted from [10].

Before proceeding with the calculation of $E(s)$, it is necessary to define the ripple coefficient ϵ and normalization constant ϵ_R. These are real-valued parameters used to scale $P(s)$ and $F(s)$, ensuring that the desired passband ripple and return loss specifications are satisfied. The ripple coefficient controls the amplitude variation in the passband and it can be found using (2.19). In contrast, the normalization constant ϵ_R scales the reflection response appropriately. For non-canonical filters ($n_{fz} < N$), the value of ϵ_R is unity, whereas for canonical filters ($n_{fz} = N$), the normalization constant must be calculated using (2.20) to maintain consistency with the prescribed ripple characteristics [10].

$$\epsilon = \frac{1}{\sqrt{10^{RL/10} - 1}} \left| \frac{P(\omega)}{F(\omega)/\epsilon_R} \right|_{\omega=\pm 1} \tag{2.19}$$

$$\epsilon_R = \frac{\epsilon}{\sqrt{\epsilon^2 - 1}} \tag{2.20}$$

The alternating poles method exploits the factorization of elements in the conservation of energy expression, allowing the denominator to be constructed from a combination of the transmission and reflection polynomials. In addition, complex factorization identities allow to expand the polynomials resulting in the following expression [10]:

$$\epsilon^2 \epsilon_R^2 E(\omega) E(\omega)^* = \left[\epsilon_R P(\omega) - j\epsilon F(\omega)\right] \left[\epsilon_R P(\omega) + j\epsilon F(\omega)\right] \tag{2.21}$$

Since $E(s)$ must satisfy the Hurwitz condition, only the poles located on the left half of the complex plane are of interest. This leads to a direct expression for $E(\omega)$ in terms of $P(\omega)$ and $F(\omega)$ which were previously found and preserves the conservation of energy property as shown in [10].

$$E(\omega) = \frac{P(\omega)}{\epsilon} - \frac{jF(\omega)}{\epsilon_R} \tag{2.22}$$

In summary, the denominator polynomial $E(s)$ provides the structural foundation that connects the transmission and reflection response of the filter. Together, the polynomials $P(s)$, $F(s)$, and $E(s)$ form a complete description of the filter response in terms of its scattering parameters. More importantly, these polynomials serve as the starting point for the synthesis of the coupling matrix, where their coefficients are systematically mapped to physical coupling elements. The next section builds upon this relationship by demonstrating how the characteristic polynomials are used to construct the coupling matrix representation of the filtering network.

2.2 Evaluated Bandpass Filter

The synthesis procedure previously described is applied here through a MATLAB implementation to determine the characteristic polynomials $P(s)$, $F(s)$, and $E(s)$ for the selected filter specifications. These polynomials define the scattering parameters of the normalized bandpass prototype and serve as the basis for the subsequent transformation into a bandstop response.

The design under consideration corresponds to a Chebyshev fourth-order bandpass filter, with a center frequency of 1 GHz, fractional bandwidth of 5%, return loss of 22 dB, and two transmission zeros located at $s = \pm j1.5699$ in the complex frequency plane. These transmission zeros are symmetrically distributed and directly control the selectivity of the filter response.

The transmission polynomial $P(\omega)$ is defined as the product of the finite transmission zeros in the frequency domain using (2.6), note that $\omega_1 = -1.5699$ rad/s, and $\omega_2 = +1.5699$ rad/s. Then, it is necessary to switch to $P(s)$ by substituting $s = j\omega$. Since the difference between the filter order and the number of transmission zeros is an even value, it is necessary to multiply $P(s)$ by j. The resulting polynomial is shown in (2.23).

$$P(s) = (1j)s^2 + (2.4646j)s^0 \tag{2.23}$$

The reflection polynomial $F(s)$ is obtained using the recursive function from the Appendix A.1, which generates vectors $U_N(s)$ and $V_N(s)$, where the roots of $U_N(s)$ are mapped into the s-domain to construct $F(s)$. The corresponding reflection polynomial is shown below.

$$F(s) = (1)s^4 + (1.0647)s^2 + (0.1594)s^0 \tag{2.24}$$

The equivalent values for the ripple coefficient and the normalization constant are found from the two polynomials above, which are evaluated at two normalized frequency points $\omega = \pm 1$ rad/s. Finally, the denominator polynomial $E(s)$ is constructed to guarantee that all poles lie in the left half of the complex plane, ensuring the Hurwitz characteristic. The resulting denominator polynomial is

$$E(s) = (1)s^4 + (2.2462)s^3 + (3.5875)s^2 + (3.2884)s^1 + (2.0072)s^0 \tag{2.25}$$

Since the transmission zeros are symmetrically located along the imaginary axis, the polynomials $F(s)$ and $E(s)$ generated from them are also symmetric. As a result, the characteristic polynomials are composed of purely real coefficients. It should also be noted that the polynomial $P(s)$ was purely real-valued before being multiplied by j due to orthogonality condition.

These evaluated polynomials will be used directly in the next section to perform the bandpass-to-bandstop transformation. In particular, the transformation is achieved by interchanging the numerator polynomials in the scattering parameters while preserving the denominator polynomial.

2.3 Bandpass-to-Bandstop Transformation

The synthesis procedure described in the previous section is used to model a bandpass filtering function based on its characteristic polynomials. These polynomials determine the scattering parameters of a lossless two-port network as defined in (2.5) and (2.7).

In a bandpass filter, the transmission polynomial $P(s)$ determines the location of the transmission zeros, while the reflection polynomial $F(s)$ represents the return loss in the passband. In contrast, the bandstop response is obtained by reversing the roles of these numerator polynomials in the scattering parameters. As a result, the characteristics of S_{21} and S_{11} are exchanged. In other words, the transmission behavior associated with the bandpass response becomes the reflection behavior in the bandstop case, and vice versa. Meanwhile, the denominator polynomial remains unchanged in order to preserve the unitary condition of a passive lossless network, as shown in (2.26) and (2.27) [11].

$$S_{21_{BSF}} = \frac{F'(s)/\epsilon_R}{E(s)} \tag{2.26}$$

$$S_{11_{BSF}} = \frac{P'(s)/\epsilon}{E(s)} \tag{2.27}$$

The characteristic polynomials for the bandstop prototype are denoted by $F'(s)$ and $P'(s)$ in order to distinguish them from the bandpass polynomials $F(s)$ and $P(s)$. When comparing the characteristic polynomials, two important observations should be made. The first one is that $F'(s)$ must satisfy the orthogonality condition detailed in Table 2.1. Since $(N - n_{fz})$ is even, the corresponding condition is applied to $F'(s)$ instead of $P(s)$, which introduces a factor of j. Therefore, $F'(s)$ is obtained directly from $F(s)$ multiplied by j.

$$F'(s) = (1j)s^4 + (1.0647j)s^2 + (0.1594j)s^0 \tag{2.28}$$

The second consideration is that the resulting polynomial $P(s)$ in the bandpass prototype already includes the factor of j. Hence, the corresponding polynomial for the bandstop case is obtained by removing this factor. In other words, dividing $P(s)$ by j, gives the resulting polynomial $P'(s)$

$$P'(s) = (1)s^2 + (2.4646)s^0 \tag{2.29}$$

These two observations apply specifically to the characteristic polynomials derived previously. More generally, for the bandstop prototype, the same polynomial synthesis conditions are retained, and the characteristic polynomials can be obtained directly through the same synthesis procedure. The only modification is that the condition associated with $P(s)$ in Table 2.1 is instead applied to $F(s)$, consistent with the exchange of the numerator polynomials while preserving the transmission behavior.

In addition, the denominator polynomial $E(s)$ remains unaltered, preserving the pole distribution, filter order, and selectivity in the transformation from the bandpass prototype to its equivalent bandstop form. Likewise, the ripple coefficient and normalization constant remain unchanged.

The MATLAB code in Appendix A.2 was developed to illustrate the bandpass-to-bandstop transformation. In this implementation, the bandpass prototype is defined by specifying some parameters such as the filter order n, rejection loss RL, number of transmission zeros n_{fz}, and the location of those transmission zeros in the normalized frequency complex plane.

This operation effectively exchanges the transmission and reflection characteristics of the network, which translates into the signal transitioning from the passband to the stopband, and vice versa. From the physical standpoint, this transformation relocates the transmission zeros, causing the frequencies to move from minimal attenuation to exhibit a stopband behavior. Similarly, frequencies which were originally attenuated become the passband of the bandstop filter. This behavior can be observed in Figure 2.5, where the bandpass prototype used is the one corresponding to the symmetrical function described before.

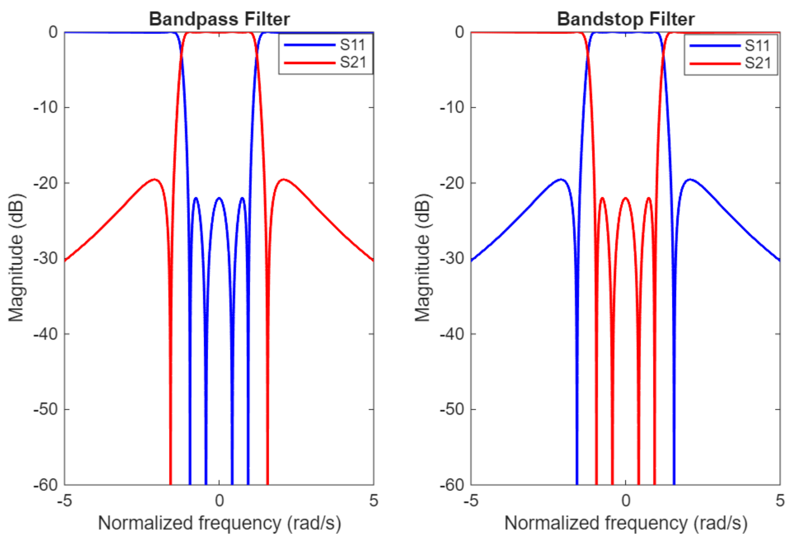

Figure 2.5: Bandpass to Bandstop Transformation

The resulting bandstop polynomials can then be used as the basis for coupling matrix synthesis, where the modified transmission and reflection characteristics are represented by physical coupling elements. This process is described in the following section.

2.4 Coupling Matrix Synthesis and Topology Transformation

In RF microwave filter design, the coupling matrix provides a mathematical representation of how resonant elements interact with one another and with the input and output ports. Each diagonal entry of the matrix corresponds to a resonator's self coupling (its resonant frequency and external quality factor), while each off diagonal entry represents the mutual coupling between a pair of resonators (how energy transfers between them). By adjusting these matrix entries, we can shape the filter's center frequency, bandwidth, and shape. In practice, after deriving the coupling matrix for a particular filter, its values can be translated into physical dimensions in microstrip structures.

The coupling matrix in RF microwave filters is a mathematical approach that simplifies filter design through matrix operations such as inversion, transformation and partitioning. Also, this technique allows effective simulation of complex filters.

In the following subsections, a bandpass filter and its corresponding coupling matrix are first synthesized, and the resulting response is then compared with that of the equivalent bandstop filter.

2.4.1 Direct Synthesis of the Coupling Matrix

The coupling matrix representation was introduced in 1970 by Atia and Williams [12]. It provides a convenient network-based description of a microwave filter in terms of the interactions among its resonating elements and terminal ports. In this formulation, the filter is modeled as a set of coupled resonators, where off-diagonal terms describe the mutual coupling between resonators, including both mainline and cross-coupling paths, while the diagonal terms account for the self-coupling of each resonator, often associated with frequency-invariant reactances introduced to realize more general filtering characteristics. This representation is especially useful because it establishes a clear link between the desired filtering function and a realizable circuit topology [13].

Within this framework, the transfer and reflection characteristics obtained from polynomial synthesis provide the basis for determining the coupling matrix. The main idea is to derive the two-port admittance parameters of the network and use them to relate the coupling coefficients to the synthesized transfer and reflection polynomials.

The admittance polynomials can be found from the characteristic polynomials using the following relations [10]:

For N even:

$$y_{21} = \frac{y_{21_n}(s)}{y_d(s)} = \frac{P(s)/\epsilon}{m_1(s)} \tag{2.30}$$

$$y_{22} = \frac{y_{22_n}(s)}{y_d(s)} = \frac{n_1(s)}{m_1(s)} \tag{2.31}$$

For N odd:

$$y_{21} = \frac{y_{21_n}(s)}{y_d(s)} = \frac{P(s)/\epsilon}{n_1(s)} \tag{2.32}$$

$$y_{22} = \frac{y_{22_n}(s)}{y_d(s)} = \frac{m_1(s)}{n_1(s)} \tag{2.33}$$

where:

$$m_1(s) = Re(e_0 + f_0) + j\,Im(e_1 + f_1)s + Re(e_2 + f_2)s^2 + ... \tag{2.34}$$

$$n_1(s) = j\,Im(e_0 + f_0) + Re(e_1 + f_1)s + j\,Im(e_2 + f_2)s^2 + ... \tag{2.35}$$

Then, the residues r_{21_k} and r_{22_k} need to be extracted from the numerator and denominator polynomials ($y_{21}(s)$ and $y_{22}(s)$). Also, the eigenvalues λ_k can be found from the roots of $y_d(s)$ and dividing them by j to obtain pure real values.

Finally, the general form of the transversal filter is shown in (2.36) and (2.37), where $K_\infty = 0$ except for the fully canonical case [10].

$$Y_N = \frac{1}{y_d(s)} \begin{bmatrix} y_{11_n}(s) & y_{21_n}(s) \\ y_{12_n}(s) & y_{22_n}(s) \end{bmatrix} \tag{2.36}$$

$$Y_N = j \begin{bmatrix} 0 & K_\infty \\ K_\infty & 0 \end{bmatrix} + \sum_{k=1}^{N} \frac{1}{s - j\lambda_k} \begin{bmatrix} r_{11_k} & r_{12_k} \\ r_{21_k} & r_{22_k} \end{bmatrix} \tag{2.37}$$

In summary, the direct synthesis procedure provides the connection between the characteristic polynomials of the filtering function and its coupling matrix representation by representing the synthesized response in terms of a two-port admittance function. In the case of the bandstop filter, the same formulation is preserved, except that the transfer and reflection relationships are exchanged consistently with the interchanged numerator polynomials.

In this way, the admittance-polynomial approach converts the polynomial synthesis results into a matrix representation suitable for circuit interpretation and physical realization. These parameters are then used to determine the coupling coefficients and resonator terms of the transversal prototype.

2.4.2 Transversal Form of the Coupling Matrix

The transversal coupling matrix is obtained from the two-port short-circuit admittance parameter matrix, commonly referred to as the $N + 2$ coupling matrix. Its elements are determined from the coefficients of the characteristic polynomials associated with the transfer and reflection scattering parameters, along with the circuit elements of the transversal array network derived during the direct synthesis procedure.

For a fourth-order filter, this transversal representation is illustrated in Table 2.2.

Table 2.2: Fourth-order coupling matrix. Reproduced from [10]

	S	1	2	3	4	L
S	0	M_{S1}	M_{S2}	M_{S3}	M_{S4}	M_{SL}
1	M_{1S}	M_{11}	0	0	0	M_{1L}
2	M_{2S}	0	M_{22}	0	0	M_{2L}
3	M_{3S}	0	0	M_{33}	0	M_{3L}
4	M_{4S}	0	0	0	M_{44}	M_{4L}
L	M_{LS}	M_{L1}	M_{L2}	M_{L3}	M_{L4}	0

In the transversal topology, each resonator is coupled only to the source and load, while no direct couplings exist between resonators. As a result, the matrix contains nonzero entries only along the main diagonal, which represent the self-coupling terms, and in the rows and columns associated with the source and load, which represent the external couplings.

Furthermore, for a reciprocal lossless network, the coupling matrix is symmetric with respect to its main diagonal, such that $M_{ij} = M_{ji}$. The direct source-to-load coupling coefficient $M_{SL} = M_{LS}$ is normally zero for conventional bandpass filtering functions and becomes nonzero for canonical configurations.

Using the same bandpass prototype introduced in the previous section, the corresponding synthesized transversal coupling matrix is presented in Table 2.3. This matrix serves as the starting point for subsequent matrix transformations, through which a more practical folded topology can be obtained for physical filter implementation.

Table 2.3: Transversal coupling matrix of the bandpass prototype

	S	1	2	3	4	L
S	0	0.3435	-0.6660	0.6660	-0.3435	0
1	0.3435	1.2969	0	0	0	0.3435
2	-0.6660	0	0.8025	0	0	0.6660
3	0.6660	0	0	-0.8025	0	0.6660
4	-0.3435	0	0	0	-1.2969	0.3435
L	0	0.3435	0.6660	0.6660	0.3435	0

In addition to the bandpass transversal coupling matrix, the corresponding bandstop transversal form can be obtained from the characteristic polynomials found in the previous section. As a result, the bandstop filtering function is represented by a different transversal coupling matrix, as shown in Table 2.4.

Table 2.4: Transversal coupling matrix of the bandstop prototype

	S	1	2	3	4	L
S	0	1.0074	-0.3289	0.3289	-1.0074	1
1	1.0074	1.2969	0	0	0	1.0074
2	-0.3289	0	0.8025	0	0	0.3289
3	0.3289	0	0	-0.8025	0	0.3289
4	-1.0074	0	0	0	-1.2969	1.0074
L	1	1.0074	0.3289	0.3289	1.0074	0

A fundamental distinction in the bandstop transversal matrix is the presence of a direct source-to-load coupling term. In this case, the coefficient $M_{SL} = M_{LS}$ is no longer zero, but instead takes a unitary value under normalized conditions. This behavior follows from the fact that, after swapping the numerators, the transmission polynomial becomes an Nth-degree function. Therefore, the condition $N - n_{fz} = 0$ is satisfied, which is equivalent to the fully canonical case. The mathematical basis has been demonstrated in [10], which corresponds to the following expression

$$M_{SL} = \frac{\epsilon(\epsilon_R - 1)}{\epsilon_R} \tag{2.38}$$

where ϵ_R is unitary only for the non-canonical case.

From a physical standpoint, this direct source-to-load path is consistent with the nature of the bandstop response. In contrast to the bandpass case, where signal transmission is mainly established through the resonating path, the bandstop structure includes an additional path between source and load [14]. The interaction between this direct path and the resonant paths produces the characteristic rejection behavior of the bandstop filter. For this reason, the unitary value of M_{SL} in the transversal representation is the result of the circuit structure required to realize the bandstop response.

Using the same prototype discussed previously, the synthesized bandpass transversal coupling matrix is shown together with its bandstop counterpart in Fig. 2.6. A comparison of both configurations shows that the polynomial transformation from bandpass to bandstop not only modifies the numerical values of the coupling coefficients, but also alters the network topology through the introduction of a direct source-to-load coupling path. This observation is particularly important for the subsequent transformation into folded form, since the presence of this term must be preserved in order to obtain a practical topology consistent with the intended bandstop implementation.

(a) (b)

Figure 2.6: Transversal coupling diagram: a) Fourth-order bandpass filter, b) Equivalent bandstop filter.

2.4.3 Folded Form of the Transversal Coupling Matrix

The transversal coupling matrix is useful as an initial synthesis form, but it is generally not convenient for physical implementation. Since each resonator is directly coupled to both the source and the load, the topology becomes increasingly impractical as the filter order increases. For this reason, the transversal matrix is commonly transformed into an equivalent folded canonical form, which provides a more suitable setting for fabrication.

This transformation is realized through a sequence of similarity transformations, or rotations, that preserve the electrical response of the network while eliminating undesired coupling entries. By applying these operations systematically from right to left along rows and top to bottom along columns. Starting with the outermost rows and columns and working inward toward the center of the matrix, the transversal matrix is converted into the folded coupling form [10].

The process of transforming a transversal form to a folded one follows the process detailed below [10]:

1. Identify the matrix element to make zero, this is called the "annihilated value". The elimination sequence is followed systematically from the outer rows and columns toward the center of the matrix. The transformation process can be divided into two categories: row annihilation and column annihilation.

2. Select the pivot pair that defines the rotation region. In row annihilation, the pivot is chosen as a pair of adjacent indices ending at the annihilated element. In column annihilation, the pivot is chosen as a pair of adjacent indices beginning at the annihilated element. For each transformation, all entries associated with row i and column j of the pivot pair are modified in that rotation.

3. Compute the rotation angle and the corresponding coefficients of the rotation matrix $\mathbf{R_r}$. These quantities are determined from the entries involved in the selected annihilation step. For row annihilation, the relevant terms are taken from the same row, whereas for column annihilation they are taken from the same column. A constant c is introduced to distinguish between both cases, with $c = -1$ for row annihilation and $c = +1$ for column annihilation. Using these terms, the rotation angle θ_r is calculated from the expression in Table 2.5.

4. Build the rotation matrix R_r as an $(N+2) \times (N+2)$ identity matrix modified only at the pivot locations. For a pivot pair (i, j), the nontrivial entries are defined as $R_{ii} = R_{jj} = \cos(\theta_r)$, $R_{ij} = -\sin(\theta_r)$, and $R_{ji} = \sin(\theta_r)$. All remaining diagonal entries are equal to 1, and all other off-diagonal entries are zero.

5. Obtain the transformed coupling matrix by applying the following expression

$$\mathbf{M_r} = \mathbf{R_r} \cdot \mathbf{M_{r-1}} \cdot \mathbf{R_r^t} \tag{2.39}$$

where $\mathbf{M_r}$ is the coupling matrix from the previous step and $\mathbf{R_r^t}$ is the transpose of the rotation matrix.

The transformation steps are summarized in Table 2.5.

Table 2.5: Fourth order bandpass filter reduction of the transversal matrix to the folded configuration. Adapted from [10]

				$\theta_r = \tan^{-1}(cM_{kl}/M_{mn})$				
Transform Number	Pivot (i,j)	Element to be annihilated	$N+2$ matrix	k	l	m	n	c
1	$(3,4)$	M_{S4}	In row "S"	S	4	S	3	-1
2	$(2,3)$	M_{S3}	In row "S"	S	3	S	2	-1
3	$(1,2)$	M_{S2}	In row "S"	S	2	S	1	-1
4	$(2,3)$	M_{2L}	In column "L"	2	L	3	L	$+1$
5	$(3,4)$	M_{3L}	In column "L"	3	L	4	L	$+1$
6	$(2,3)$	M_{13}	In row "1"	1	3	1	2	-1

After applying the sequence of transformations to the transversal matrix of the bandpass prototype, the equivalent folded canonical matrix is obtained, as shown in Table 2.6.

Table 2.6: Folded coupling matrix of the bandpass prototype

	S	1	2	3	4	L
S	0	1.0597	0	0	0	0
1	1.0597	0	0.8553	0	-0.3614	0
2	0	0.8553	0	0.8559	0	0
3	0	0	0.8559	0	0.8553	0
4	0	-0.3614	0	0.8553	0	1.0598
L	0	0	0	0	1.0598	0

This transformation procedure can be applied to any coupling matrix provided that the direct cross-coupling elements are taking into consideration, since they are a fundamental part of the physical realization of the filtering function. These coupling terms are essential because they preserve the electrical characteristics of the synthesized response and later define the physical layout that must be realized in the final structure. Therefore, the same sequence of similarity transformations can be applied to the bandstop filter, yielding the folded coupling matrix shown in Table 2.7.

Table 2.7: Folded coupling matrix of the bandstop prototype

	S	1	2	3	4	L
S	0	1.4987	0	0	0	1
1	1.4987	0	0.8553	0	1.4846	0
2	0	0.8553	0	-0.8559	0	0
3	0	0	-0.8559	0	0.8553	0
4	0	1.4846	0	0.8553	0	1.4987
L	1	0	0	0	1.4987	0

The corresponding coupling diagrams provide a more intuitive interpretation of the matrix coefficients. As in the previous section, solid lines denote positive coupling coefficients, whereas the dashed line represents negative coupling coefficients. This distinction indicates that not all couplings are of the same nature.

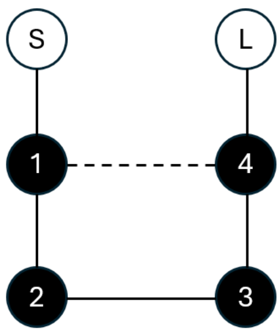

(a)

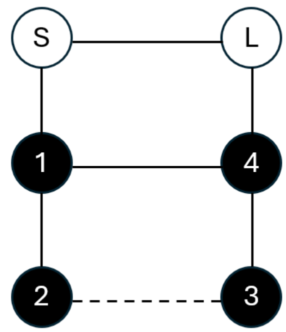

(b)

Figure 2.7: Coupling diagrams: a) 4x2 bandpass filter, b) 4x2 bandstop filter

Furthermore, the initial bandstop prototype requires a 270° direct source-to-load connection. To obtain a topology that is more consistent with the bandpass prototype, the folded coupling matrix of the bandstop filter can be further transformed by inverting the signs of the paths associated with the resonator couplings and the direct source-load coupling. This operation leads to the equivalent matrix and coupling diagram shown below, in which the direct source-load path can be represented by a 90° transmission-line section.

Table 2.8: Folded coupling matrix of the adjusted bandstop filter

	S	1	2	3	4	L
S	0	1.4987	0	0	0	-1
1	1.4987	0	0.8553	0	-1.4846	0
2	0	0.8553	0	0.8559	0	0
3	0	0	0.8559	0	0.8553	0
4	0	-1.4846	0	0.8553	0	1.4987
L	-1	0	0	0	1.4987	0

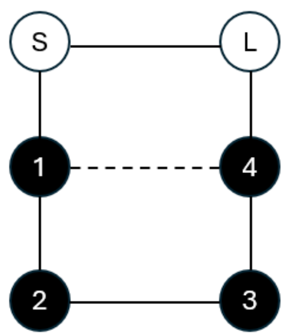

Figure 2.8: Coupling diagram of the adjusted bandstop filter

This chapter established the theoretical foundation for the synthesis of the proposed filtering responses, beginning with the characteristic polynomials and continuing through the direct generation and transformation of the coupling matrices. This synthesis procedure serves as the basis for the microstrip filter implementation developed in the next chapter, where the entries of the coupling matrix are translated into physical design parameters such as resonator dimensions, spacing, and coupling structures in order to achieve the intended microwave filter response.

Chapter 3

Microstrip Filter Implementation and Tuning

This chapter examines the resonator in greater detail as the fundamental element of the proposed bandstop filter. The main characteristics of microstrip resonators are first presented to establish the basis for the physical design. The coupling-matrix entries derived in the previous chapter are then translated into physical dimensions to realize the filter layout, which is subsequently analyzed using full-wave electromagnetic simulation before fabrication. The chapter concludes with a time-domain tuning procedure used to refine the frequency response by adjusting the physical dimensions of the structure.

3.1 Fundamentals of Resonators

Resonators are the fundamental building blocks of microwave filters, since they determine the frequency-selective behavior of the overall network. In both bandpass and bandstop configurations, the filter response is established through the interaction of resonant elements and the couplings between them. For this reason, understanding the basic properties of resonators is an essential step before proceeding to the physical implementation of the proposed microstrip filter.

In general, a resonator is a structure capable of storing electric and magnetic energy. In an equivalent lumped representation, these storage mechanisms are associated with a capacitor and an inductor respectively. The continuous exchange of energy between these two forms gives rise to resonance. At the resonant condition, the structure oscillates naturally at a specific frequency, denoted here as f_c, which can be expressed for an ideal LC resonator as

$$f_c = \frac{1}{2\pi\sqrt{LC}} \tag{3.1}$$

This expression provides a useful conceptual model for resonance. However, in practical microstrip filters, the resonators are implemented as distributed structures rather than ideal lumped elements. Therefore, the resonant frequency is ultimately determined by the physical dimensions of the resonator, the substrate properties, and any loading elements introduced for tuning.

Another important parameter is the unloaded quality factor Q_u, which describes the ability of the resonator to store energy relative to the energy dissipated in each cycle. It is an indicator of resonator loss and filter performance; for instance, a higher unloaded quality factor corresponds to lower dissipation and a sharper resonant response. Q_u can be estimated in a single resonator from a weakly coupling to the input/output as described in [15]:

$$Q_u = \frac{Q_L}{1 - |S_{21}|} \quad \forall \quad |S_{21}| < -20dB \tag{3.2}$$

where the loaded quality factor is given by

$$Q_L = \frac{1}{FBW} \tag{3.3}$$

The loaded quality factor depends on both the intrinsic losses of the resonator and the external loading introduced by the feeding structure, while the unloaded quality factor represents only the internal resonator losses. For this reason, Q_u is commonly used to evaluate the intrinsic performance of a resonator before integrating it into a complete filter network.

Besides the resonant frequency and quality factor, the physical geometry of the resonator also plays a major role in filter design. In microstrip technology, the shape of the resonator influences size, coupling strength, fabrication simplicity, and tuning capability. These aspects are especially important in compact and tunable filters, where the resonator must not only satisfy the electrical requirements but also allow practical physical implementation.

For the present work, special attention is given to the hairpin-line resonator, since it provides a compact and widely adopted microstrip configuration suitable for filter implementation [16, 17]. Its geometry enables practical realization of the required coupling relationships while maintaining reduced circuit size. The following subsection introduces the main characteristics of the hairpin-line resonator and explains its relevance to the proposed design.

3.1.1 Hairpin-line Resonator

Hairpin-line resonators are a practical choice for implementing compact microstrip bandstop filters. A hairpin resonator can be understood as a half-wavelength resonator that has been folded into a U-shaped structure in order to reduce the required circuit area compared to a conventional parallel-coupled line filter. This folding process makes the resonator more compact, but it also changes the electromagnetic interaction between adjacent resonators. In particular, reducing the coupled-line length tends to weaken the coupling, while the close spacing between the two arms of the same resonator introduces additional internal coupling effects. For this reason, the design of hairpin-based filters usually requires full-wave electromagnetic simulation to accurately capture these interactions [9].

Based on this concept, a tunable open-loop resonator can be developed without requiring via-hole connections to ground. This feature is especially attractive in tunable microwave filters, since it allows the resonant frequency, and therefore the filter center frequency, to be adjusted through capacitive loading. Fig 3.1 illustrates the transformation from a capacitively loaded transmission-line resonator into an equivalent open-loop resonator [9].

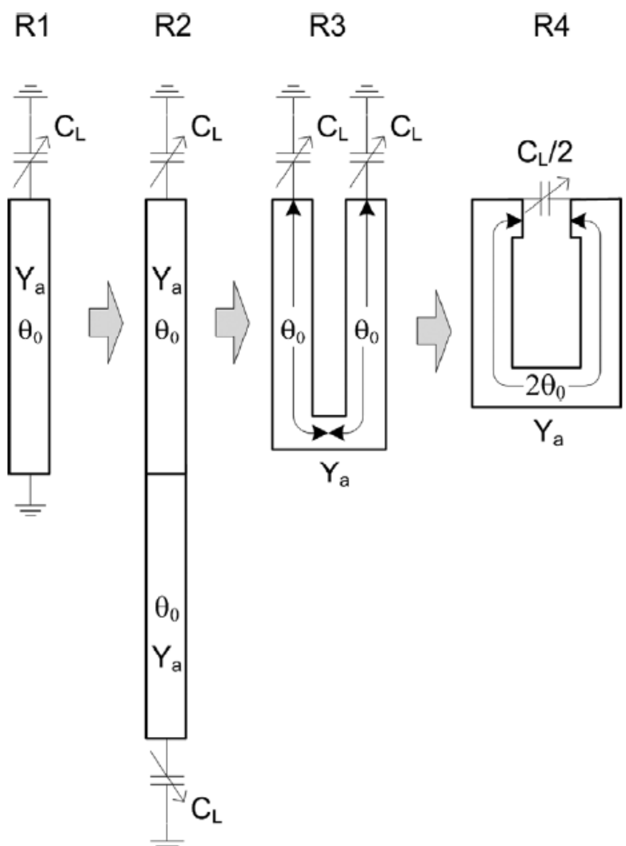

Figure 3.1: Evolution of tunable open-loop or hairpin resonator without via-hole grounding. Reproduced from [9]

As shown in Fig 3.1, resonator R1 is a single transmission-line section loaded by a capacitor. Around its fundamental resonant frequency, this resonator can be transformed into resonator R2 with equivalent electrical behavior. This occurs because at resonance, the midpoint of resonator R2 behaves as a virtual ground. Because of this virtual ground condition, the resonator can be folded into the U-shaped structure shown as resonator R3 without significantly changing its response near resonance.

In resonator R3, the capacitors located at the two open ends are electrically equivalent to a series combination. Therefore, the physical grounding used in the previous configurations is no longer required. This leads to resonator R4, which is the final tunable open-loop resonator. The resulting structure preserves the desired tuning behavior while offering a compact geometry that is more suitable for planar microstrip filter implementation.

3.1.2 Advantages and Limitations of Microstrip Filters

Several practical advantages of using microstrip filters are the reason of their widespread use in microwave systems. Their planar geometry allows them to be fabricated using standard printed-circuit techniques, which reduces manufacturing cost and facilitates mass production. They are lightweight, compact, and easily integrated with other planar components such as bias circuits. In addition, their physical dimensions can be directly adjusted to realize specific resonant frequencies and coupling conditions, making them especially suitable for filter tuning.

Despite these advantages, microstrip filters also present important limitations. Because the electromagnetic fields are partly exposed to the surrounding air, they are more vulnerable to radiation loss, dispersion, and environmental effects than enclosed waveguide structures. Their performance can also degrade at high frequencies due to conductor loss, dielectric loss, surface-wave excitation, and fabrication tolerances. As a result, microstrip implementations generally exhibit lower unloaded quality factor than cavity or waveguide filters.

In terms of quality factor, a high-Q resonator stores energy efficiently and exhibits lower loss, sharper selectivity, and better filtering performance. Conversely, a low-Q resonator has higher loss and usually leads to broader and less selective responses. Therefore, Q serves as a useful metric for assessing the tradeoff between compactness, manufacturability, and electrical performance in planar microwave filters.

Overall, microstrip technology provides an effective platform for the realization of planar microwave filters when moderate loss, compact size, and fabrication simplicity are prioritized. For this reason, it is especially well suited for the physical implementation of the filter structures developed in this work.

3.2 Physical Implementation of Coupling Matrix

3.2.1 Inverter-based Circuit

One of the main advantages of coupling matrix synthesis is that the coupling coefficients can be translated into an equivalent circuit representation, providing a practical starting point for the filter design. Before moving to the physical microstrip implementation, it is useful to construct an ideal circuit model based on admittance inverters. This intermediate step establishes a direct connection between the mathematical synthesis and the expected electrical behavior of the filter, allowing the response to be verified in circuit simulation before introducing the complexities of a physical layout.

In this representation, the admittance inverters model the main-line and cross-coupling shown in last chapter. Their role is especially important because they provide a convenient way to transform the coupling matrix coefficients into an equivalent network in which energy exchange between resonators can be clearly interpreted. For this reason, inverter-based circuits are commonly used as an intermediate synthesis stage in microwave filter design.

The inverter-based network is represented by admittance inverters, parallel L-C and FIRs. The admittance inverters, also known as J-inverters define the interaction between resonators, whether is direct coupling between adjacent resonators or cross-coupling between nonadjacent resonators. The parallel tank of inductors and capacitors models the natural resonance behavior of the resonant element, whereas the frequency-invariant accounts for the self-coupling. Together, these elements create an ideal circuit model whose response is determined by the previously synthesized coupling coefficients.

Figure 3.2 shows the inverter-based circuits implemented in Microwave Office AWR for both the ideal bandpass and bandstop filters. These two topologies are closely related because both are derived directly from the folded coupling matrix obtained in the previous chapter. For this reason, the inverter signs are preserved in the circuit representation, since they indicate the nature of the coupling required by the synthesized network. Moreover, the diagonal terms are zero due to the symmetry properties of the folded coupling matrix, hence, FIRs are not required in this circuit.

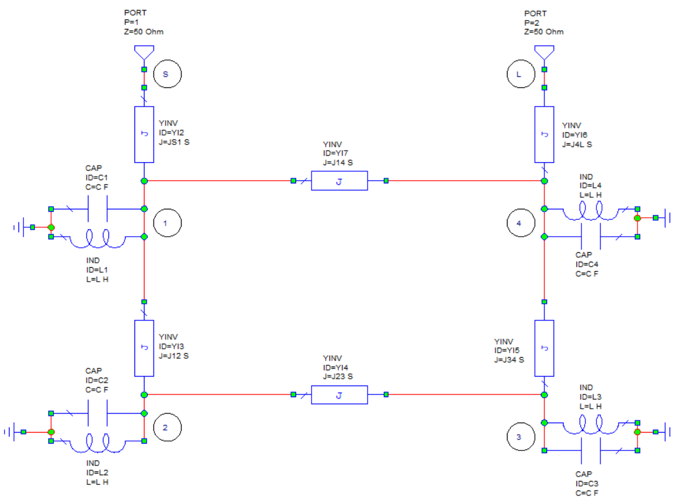

(a)

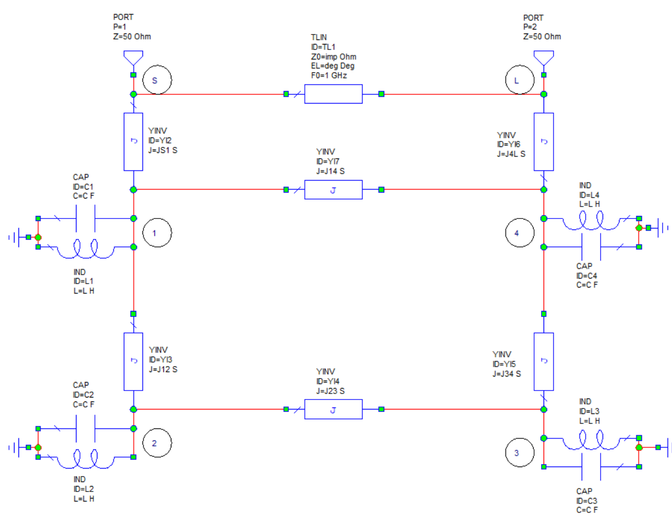

(b)

Figure 3.2: Filter representation using admittance inverters: a) Ideal bandpass filter, b) Ideal bandstop filter.

The main structural difference between the two circuits is that the bandstop configuration includes an additional direct path between source and load, represented by a 90° transmission line. As demonstrated in [5, 4, 18, 19] the direct source-to-load path is essential for generating the bandstop response and constitutes the key modification that distinguishes the bandstop circuit from its bandpass counterpart. This feature is especially important because it later provides the conceptual basis for the physical microstrip realization of the bandstop filter.

Therefore, the inverter-based circuit is not only a validation tool for the synthesized coupling matrix, but also an essential tool when comparing the actual response of the filter for tuning purposes. It provides physical insight into how the coupling coefficients are represented by circuit elements and clarifies how the bandpass and bandstop responses emerge from closely related coupling structures before the design is translated into a practical microstrip filter design.

3.2.2 Single Resonator Design

A commonly starting point in the design procedure of a filtering function is the analysis and simulation of a single resonator. Analyzing the individual resonator provides an initial understanding of its resonant behavior and demonstrates its tunable characteristics by varying the capacitance value. This step establishes a foundation for the design of the complete filter structure.

The resonator dimensions are determined based on the guided wavelength λ_g of the microstrip structure. This value can be calculated using (1.1) and (1.2), along with the substrate parameters and the width of the 50 Ω transmission line. These expressions provide an initial estimate of the resonator dimensions. The calculated physical length is then refined through EM simulation to obtain the desired resonant frequency.

The open-loop resonator was designed following the procedure described in [9], resulting in an approximate length of 0.34 λ_g to achieve resonance at 1 GHz on a 30 mil Rogers RO3003 substrate. This structure was then modeled and simulated in Ansys HFSS, as illustrated in the following figure.

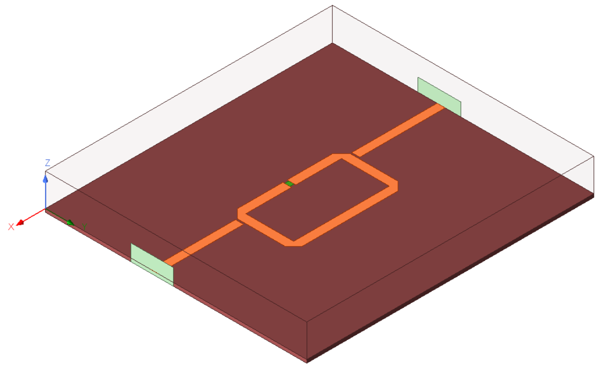

Figure 3.3: Single Resonator

The resonant behavior of the structure was evaluated for different capacitance values in order to verify its tuning capability. As the capacitance was varied from 0.66 pF to 0.95 pF, the resonant frequency shifted accordingly, producing a tuning range of 8.8% around the center frequency, as shown in Fig. 3.4. This result confirms that the proposed resonator is suitable for tunable filter applications and provides the frequency agility required for the proposed design.

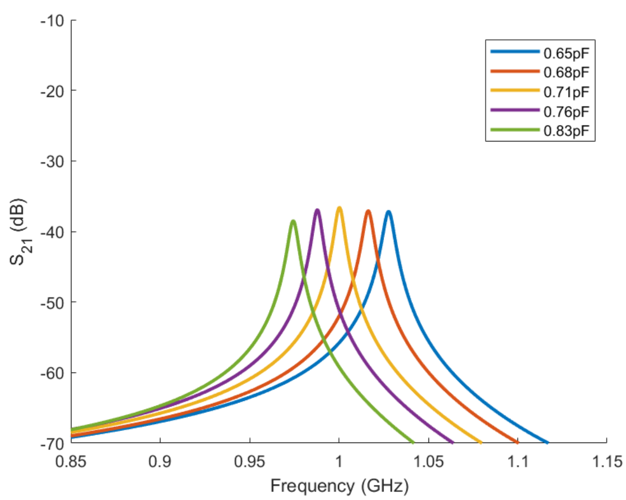

Figure 3.4: Single Resonator

The unloaded quality factor Q_u as an indicator of the filter performance, was calculated using the expressions from the last chapter. In Fig. 3.5 the unloaded Q behavior is illustrated.

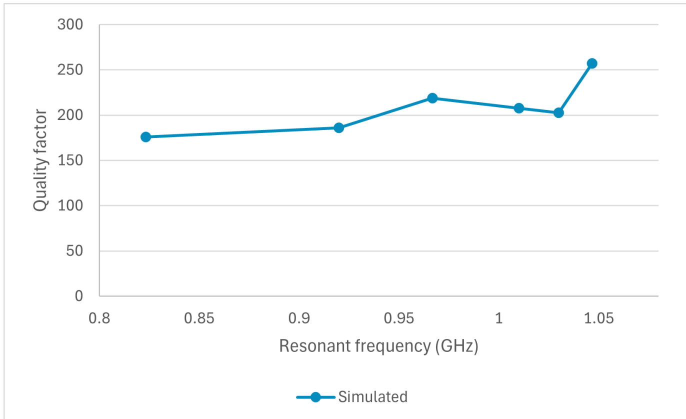

Figure 3.5: Unloaded Q for a single resonator simulated in HFSS

Generally, the single resonator analysis establishes the initial physical dimensions and validates the tuning mechanism of the proposed structure. Once the resonant response has been verified, the next step is to evaluate its external quality factor Q_e using the coupling coefficient matrix and filter parameters.

3.2.3 External Quality factor realization

The external coupling is set by the external quality factor of the input/output resonator, which are equal in this project due to the symmetry of the structure. For the extraction of the external quality factor to a singly loaded resonator, it can be extracted from a one-port configuration in which the resonator is coupled and terminated to an open end. Hence, the external Q can be calculated by taking the inverse of the fractional bandwidth.

$$Q_{ext} = \frac{f_c}{f_b - f_a} \tag{3.4}$$

where f_0 is the center frequency of the resonator, the coefficients f_a and f_b correspond to the change in the phase of the reflection coefficient at $\pm 90^{\circ}$. Fig. illustrates this difference in the calculation of Q_{ext} for the bandstop prototype.

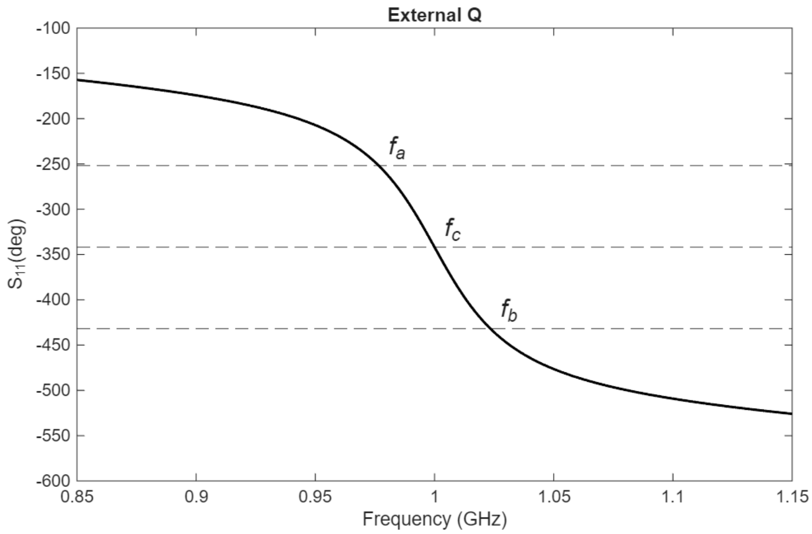

Figure 3.6: One port mode for extracting Q_{ext}. Adapted from [9]

Also, an alternative approach to calculating the external quality factor is by using the maximum of the group delay response from the reflection S_{11} [20].

$$Q_{ext} = \frac{\pi f_0 \tau_{S_{11}}(f_0)}{2} \tag{3.5}$$

where $\tau_{S_{11}}(f_0)$ is the maximum peak of the S_{11} group delay, and f_0 is the resonant frequency where this maximum occurs. The group delay is defined as

$$\tau_{S_{11}}(f_0) = -\frac{\partial(\angle S_{11})}{\partial f}\bigg|_{f=f_0} \tag{3.6}$$

Also, it has been illustrated below in Fig. 3.7

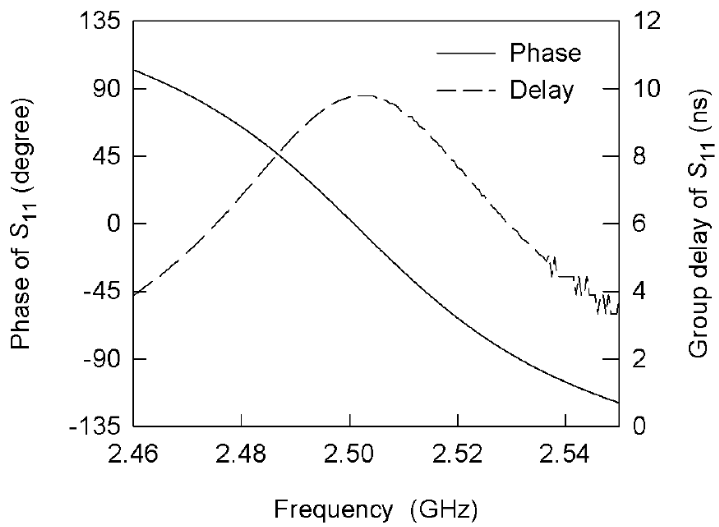

Figure 3.7: Extraction of external coupling from group delay. Reproduced from [9]

In the theoretical analysis, as demonstrated in [9], the value of Q_{ext} can be calculated from the coupling matrix coefficient M_{S1} and the fractional bandwidth as follows

$$Q_{ext} = \frac{1}{FBW} \frac{1}{|M_{S1}|^2} \tag{3.7}$$

For resonator theory, there are two alternatives to achieve an external coupling between the input/output and the outermost resonators, these are tapped-line and coupled-line, as illustrated in Fig. 3.8

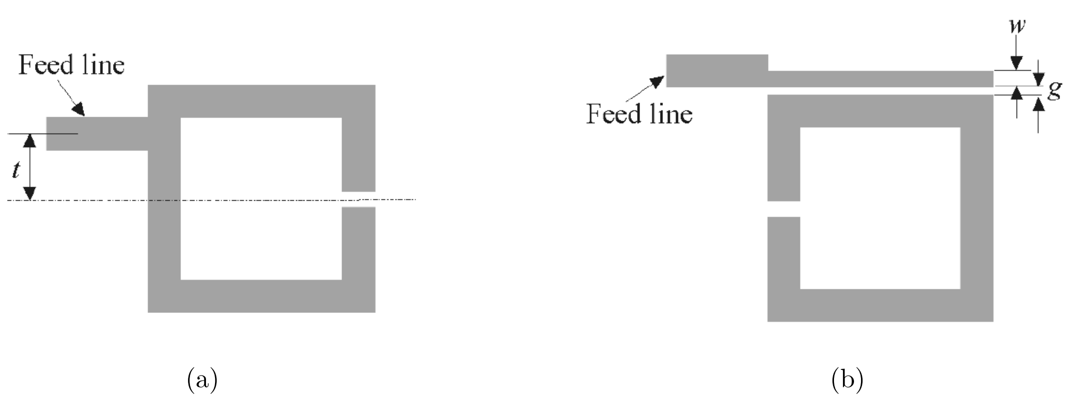

Figure 3.8: Coupling structures: a) Tapped-line coupling, b) Coupled-line coupling. Reproduced from [9]

The tapped-line connects the feed line directly to a point t along the resonator and Q_{ext} is adjusted by changing the position of t, whereas the coupled-line has a gap labeled as g between the feed line of width w and the first/last resonator, the Q_{ext} is then controlled by adjusting the gap.

In this project, tapped-lined was chosen as the coupling mechanism because it provides a stronger coupling, which is necessary to achieve the external coupling value calculated.

3.2.4 Coupling mechanisms

Before analyzing the coupling between adjacent resonators, it is practical to identify some typical coupling structures for open-loop resonators. In this type of mechanism, the coupling behavior is classified as electric, magnetic, or mixed. This classification depends mainly on the relative position of the resonators, particularly the spacing s between them and, when applicable, the offset d. These effects arise from the fringing fields surrounding each resonator [9].

The dominant type of coupling whether electric or magnetic, depends on which sides of two resonators are placed close to each other. When the open-gap region face each other, the electric field is dominant, producing electric coupling, as shown in Fig. 3.9(a). On the other hand, when the sides with the strongest magnetic field are brought into proximity, the coupling becomes mainly magnetic, as observed in Fig. 3.9(b). A third distribution is possible, when the electric and magnetic fields contribute significantly to the interaction between the resonators, this is called mixed coupling, illustrated in Fig. 3.9(c) and Fig. 3.9(d) [9].

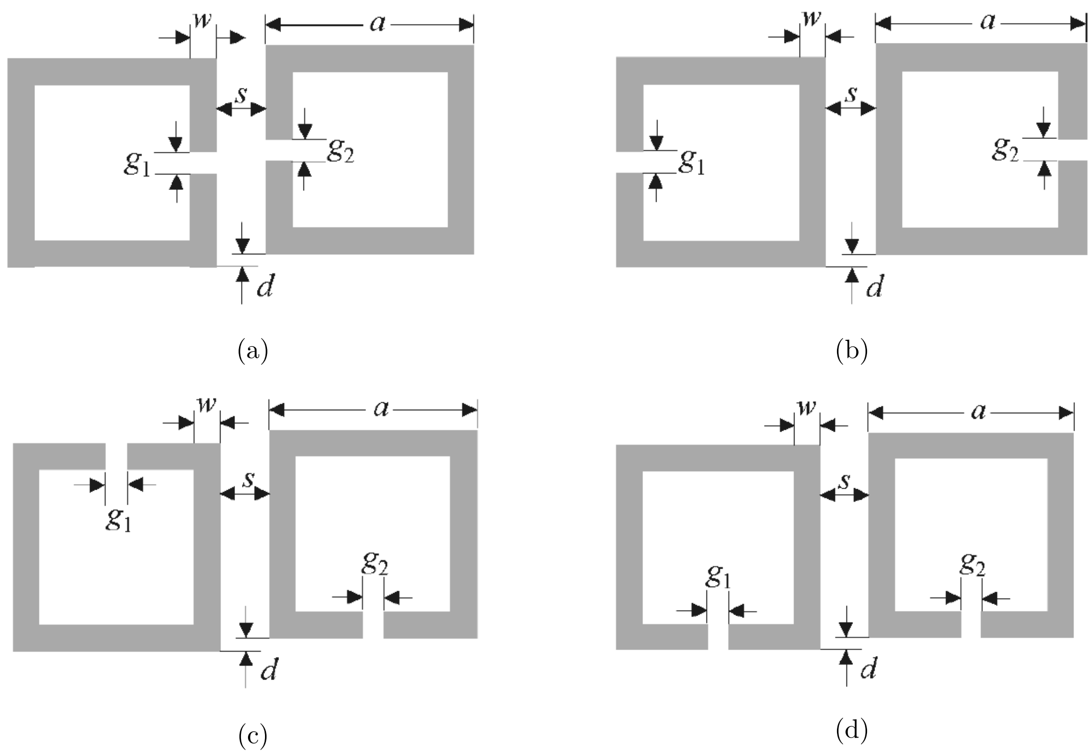

Figure 3.9: Typical coupling structures of coupled resonators with a) electric coupling, b) magnetic coupling, and c-d) mixed coupling. Reproduced from [9]

The differences among these coupling structures can be directly related to the physical orientation of the resonators through the sign of the coupling coefficients. In practice, the sign of each coefficient indicates the nature of the coupling to be implemented, allowing a distinction between structures dominated by electric coupling and those dominated by magnetic coupling. For the proposed design, the three coupling mechanisms described above are employed as part of the filter layout. This provides a clear physical interpretation of the positive and negative entries in the coupling matrix and establishes a direct relationship between the synthesized coupling values and the resonator orientation used in the bandstop filter.

3.2.5 Inter-resonator coupling

The inter-resonator coupling is responsible for controlling the bandwidth and shape of the filter. The analysis consists on using electric and magnetic wall symmetry to find the even and odd resonances (f_e and f_o), the coupling is then determined from the knowledge of the two resonant frequencies of the two individual resonators [21] as shown in Fig. 3.10.

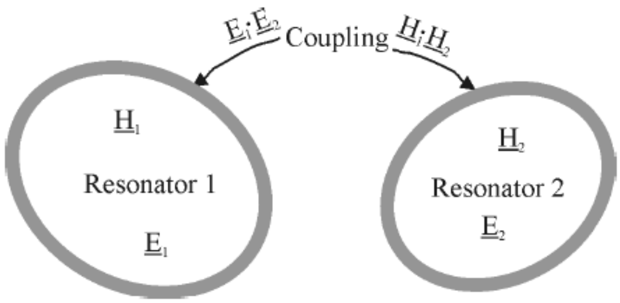

Figure 3.10: General coupled RF/microwave resonators. Reproduced from [9]

where E is the electric field and H is the magnetic field. Now, a more traditional notation for the coupling coefficient will be used as denoted by k instead of M_{ij}

Using this approach to extract k and by full-wave EM simulation, to find some characteristic frequencies associated with the coupled RF/microwave resonators. The corresponding expression to find the physical structure of coupled resonators can be defined as

$$k = \frac{f_e^2 - f_o^2}{f_e^2 + f_o^2} \tag{3.8}$$

where f_e and f_o are the peak frequency values resulting from the coupling shifting the frequency off the natural resonant frequency, corresponding to the even and odd mode analysis respectively. The stronger the coupling, the farther apart the frequency peaks, and vice versa.

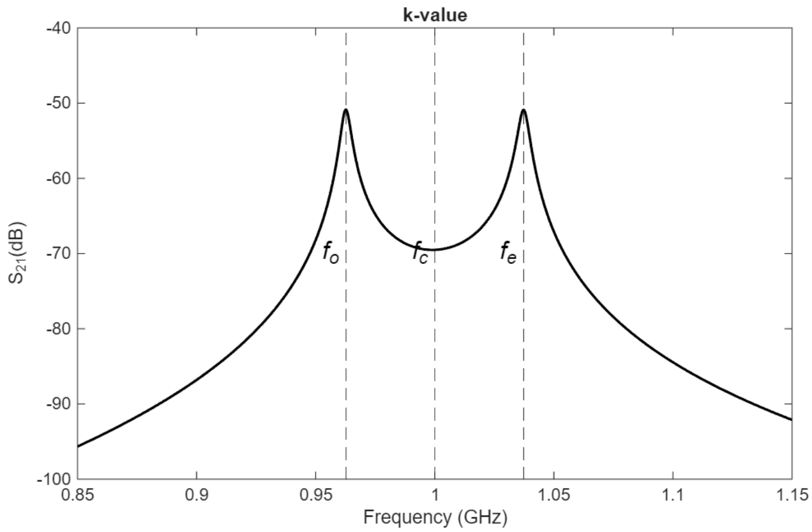

Figure 3.11: Extraction of inter-resonator coupling coefficient. Adapted from [9]

The expression to calculate the coupling coefficient k using the coupling matrix follows as

$$k_{ij} = \Delta M_{ij} \tag{3.9}$$

where Δ is the fractional bandwidth and M_{ij} is the coefficient from the coupling matrix. This is the theoretical value that will serve as the comparison to the one found using EM simulation.

The close relation between the bandpass prototype and the intended bandstop filter results in the same coupling coefficients for M_{12}, M_{23} and M_{34} which corresponds to the coupling between adjacent resonators. However, the coupling coefficient for M_{14} changes in magnitude, this last one represents the cross-coupling.

It can be observed that (3.9) applies for all coupling forms between resonators including cross-coupling and is a key step to achieve the intended filter response.

3.2.6 Design curves and parametric simulations

The physical dimensions, including the separation between the resonators were found following the procedure detailed above.

The tapped-line was simulated using only the source and the first resonator, since the filtering function is symmetric, this results in the same external coupling for the last resonator and the load ($M_{S1} = M_{4L}$). The value of t was adjusted to control Q_{ext} and the schematic used to perform the simulation is shown below.

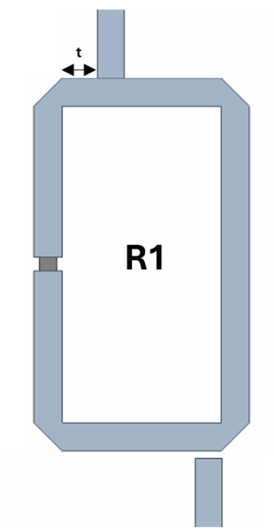

Figure 3.12: Extracting Q_{ext}. Adapted from [9]

The cross-coupling k_{14} was found adjusting the value of the separation g_{14} between the resonators 1 and 4. Note that the dimensions of the resonator were adjusted to achieve symmetry according to Fig. 3.11. Moreover, the same dimensions must be taken into account to find the value of t for the tapped-line, because the resonator's dimension must be consistent. Fig. 3.13 illustrates the setting to extract the coupling coefficient. Also, magnetic coupling was used here because a strong coupling was needed to match the theoretical value.

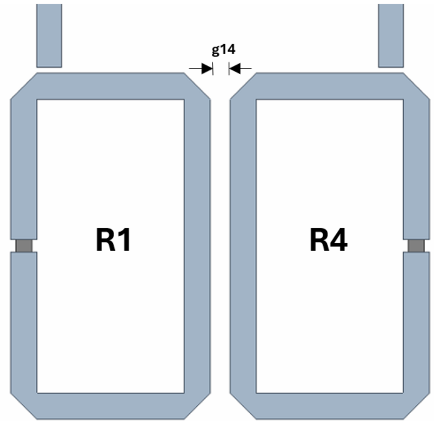

Figure 3.13: Extracting coupling coefficient k_{14}. Adapted from [9]

The inter-coupling represented by k_{23} has opposite sign compared to k_{14}. Hence, electric coupling was used to extract the coefficient. The dimensions of resonators 2 and 3 had to be adjusted to account for the symmetry around the resonance and its extraction can be observed in Fig. 3.14.

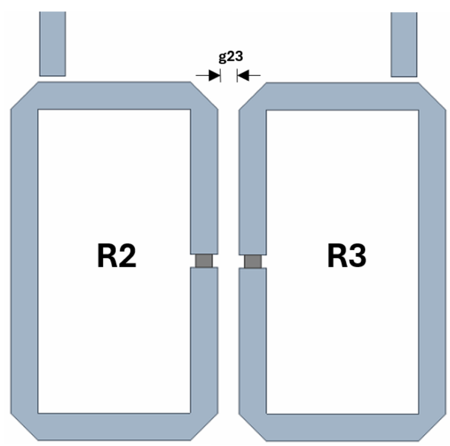

Figure 3.14: Extracting coupling coefficient k_{23}. Adapted from [9]

Finally, the coupling coefficients $k_{12} = k_{34}$ are found using Fig. 3.15, it should be mentioned that an offset d was calculated to account for the difference between the spacing g_{14} and g_{23}, for that reason this coupling was calculated at the end.

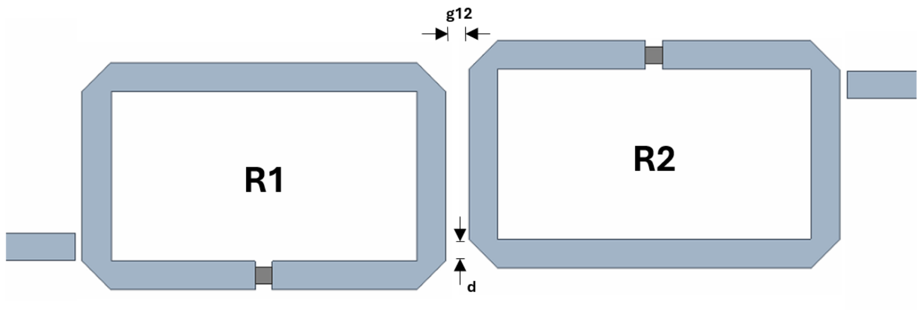

Figure 3.15: Extracting coupling coefficient k_{12} and k_{34}. Adapted from [9]

The tables below summarize the theoretical values compared to the ones extracted from the simulation.

Table 3.1: Comparison between calculated and simulated values for external coupling

Type of coupling	Coefficient	Calculated	Simulated
Tapped-line	Q_{ext}	8.9043	8.9150

Table 3.2: Comparison between calculated and simulated values for inter-coupling

Type of coupling	Coefficient	Calculated	Simulated
Electric	k_{23}	0.0428	0.0427
Magnetic	k_{14}	0.0742	0.0744
Mixed	k_{12}, k_{34}	0.0428	0.0430

Finally, the frequency response was simulated using the dimensions obtained from the coupling extraction and the external quality factor. Although the full-wave EM response exhibits the expected bandstop behavior, differences remain with respect to the inverter-based model, indicating that additional adjustment is required. Therefore, it is necessary to continue fine-tuning the dimensions of the filter in order to improve the response of the filtering function. A popular technique to achieve this is "time-domain tuning", which is presented in the following section.

3.3 Time domain analysis for filter tuning

Time-domain filter tuning was introduced by Philip Dunsmore [22] as a solution to create a desired transfer function by adjusting elements in the filter. This technique analyzes the time-domain response by taking the windowed Inverse Discrete Fourier Transform (IDFT) of the S_{11} frequency response. Given this frequency response, the time-domain method can give valuable insight into which resonator or coupling is mistuned, as well as the direction of the required correction.

Additionally, an extensive explanation about the time-domain tuning procedure is presented in [23], where the author also provides the corresponding MATLAB code to implement this technique. The first step is to understand the graph representation of the windowed function where the "null" symbolizes each resonator and the "hump" represents the coupling. In Fig. 3.16, k_{01} symbolizes the input coupling, $k_{i,i+1}$ the inter-coupling, and $k_{n,n+1}$ the output coupling as illustrated in Fig. 3.16.

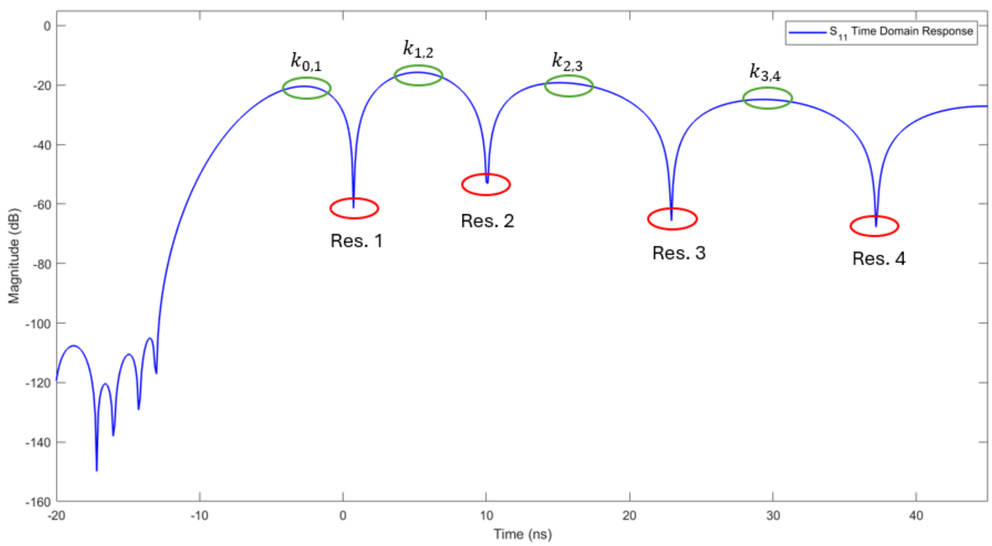

Figure 3.16: Time domain transform. Adapted from [23]

Also, the group delay representation dictates in which direction is necessary to tune the resonator, if the resonator is above the center frequency, the resonator will be located in the positive axis, but if the resonator is below the center frequency, its representation in the graph will be in the negative axis. In Fig. 3.17 a graphical representation of the group delay response is presented.

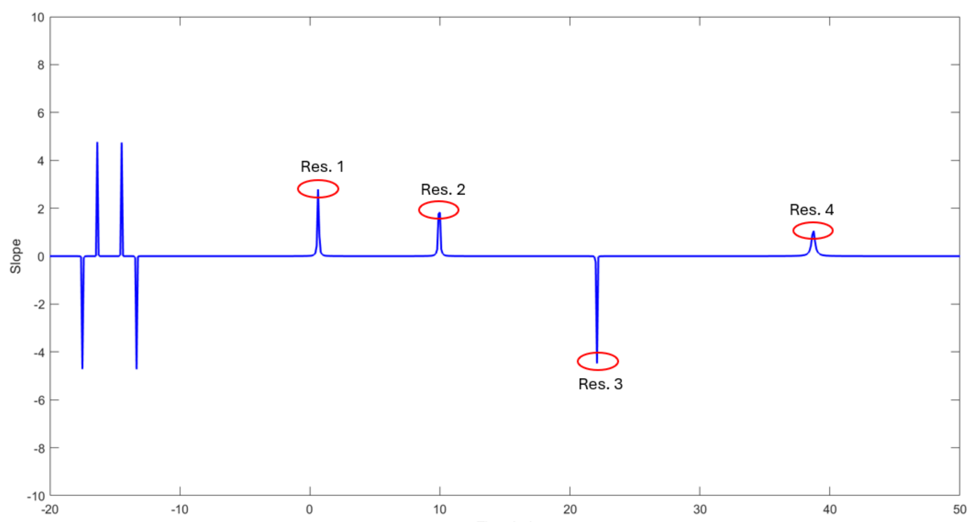

Figure 3.17: Group delay of time domain transform. Adapted from [23]

After presenting the theoretical foundation of time-domain tuning, its application to the proposed filter is now illustrated in Fig. 3.18, which compares the initial full-wave EM response, obtained from the dimensions extracted using the coupling coefficients, with the fine-tuned response after applying time-domain tuning. As observed in the figure, the tuning process improves the stopband characteristics and the out-of-band passband behavior, both characteristics are essential to approach the desired filtering response. A more detailed comparison between the microstrip implementation and the inverter-based model is provided in the next chapter.

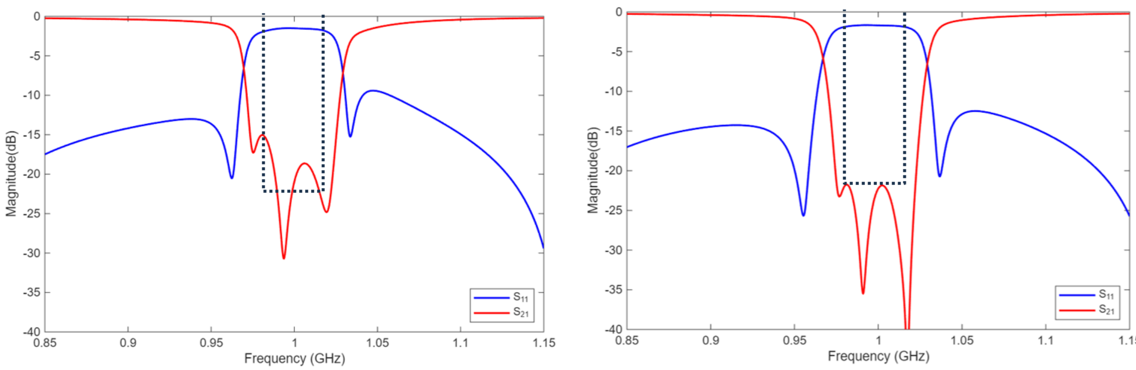

(a) (b)

Figure 3.18: Microstrip bandpass filter a) before applying time-domain tuning, b) after applying time-domain tuning

It is essential to note that the cross-coupling is not explicitly represented in the time-domain response as the adjacent inter-resonator couplings. Although it does not produce an isolated feature as easily identifiable in the graph, its variation affects the overall response and can be used as an additional parameter during tuning, for instance, in this work was used particularly to improve the alignment of the last two resonators. Based on this observation, the time-domain tuning procedure followed in this project is summarized as follows:

1. Identify the scattering parameter under study. For a bandpass filter, S_{11} provides a more suitable basis for time-domain tuning, whereas for a bandstop

filter, S_{21} is preferred. This choice is related to the parameter that more clearly emphasizes the dominant features of the desired response, such as resonator alignment and coupling effects.

2. Start by tuning all resonators to their corresponding resonant frequencies, following the procedure described in [23].

3. Tune the first external coupling, represented by k_{01}, until its response matches the ideal curve as closely as possible.

4. Continue the tuning process by adjusting resonator 1, followed by coupling k_{12}, and then resonator 2.

5. Next, tune k_{23} to its corresponding inter-resonator spacing along with the cross-coupling term until both couplings k_{23} and k_{34} approach the ideal response.

6. Conclude the procedure with a final overall adjustment of the resonators and coupling elements, including the cross-coupling k_{14}.

The final tuned response in the time domain is shown in Fig. 3.19, exhibiting a frequency response that is closer to the desired design. MATLAB was used to implement the time-domain tuning by comparing the response of the proposed microstrip filter with the inverter-based reference model. This procedure was realized initially using the Microwave Office design and was subsequently extended to the Ansys HFSS model, where further tuning was required to account for full-wave electromagnetic effects.

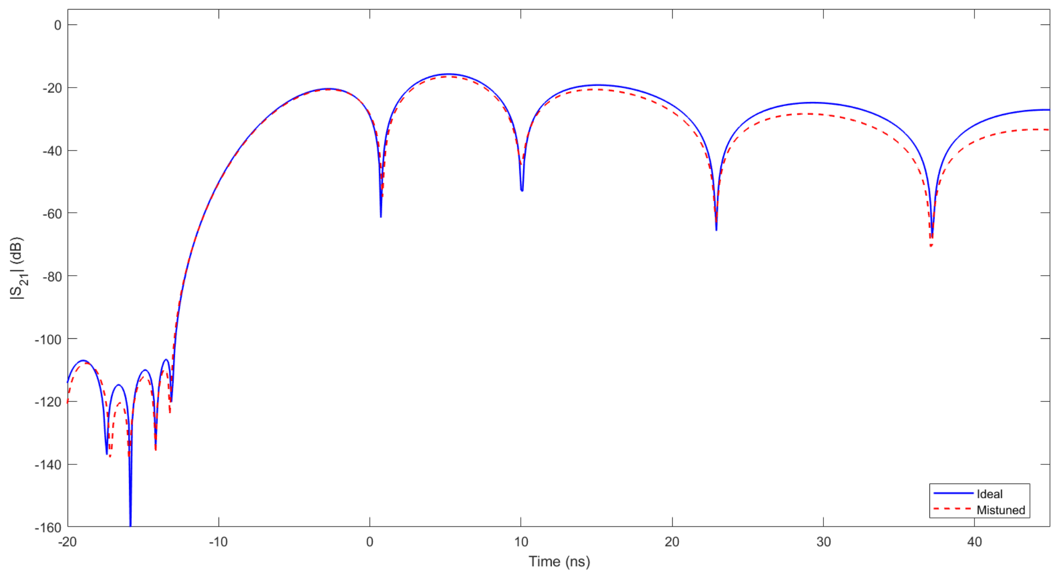

Figure 3.19: Time-domain tuning applied to the bandstop filter

The time-domain tuning plays an important role as an intermediate step between the simulation and the physical realization of the filter. This method provides a practical way to identify mistuning and refine the structure before fabrication. In this way, it helps to bridge the gap between the ideal inverter-based model and the full-wave EM implementation, leading to a response closer to the intended design. With the tuning process completed, the next chapter presents the fabrication of the proposed filter and discusses the corresponding measured results.

Chapter 4

Filter Design and Results

This chapter presents the main steps involved in the fabrication of the proposed tunable bandstop filter. This procedure includes the implementation of a DC biasing circuit to provide the voltage required to adjust the capacitance of the varactor diode. The chapter continues by verifying the single-resonator behavior and its tuning range, and then proceeds to the analysis and fabrication of the bandstop prototype.

4.1 Biasing Circuit

The incorporation of varactor diodes introduces an additional design constraint, since their capacitance is not constant but varies as a function of the applied reverse-bias voltage. Therefore, the desired capacitance value can only be achieved by establishing an appropriate DC voltage across the terminals of the varactor. As a result, the biasing network must be physically integrated into the RF filter structure in a way that enables capacitance tuning while minimizing disturbance to the microwave response.

According to [9], a DC biasing circuit can be integrated into the filter following the configuration shown below.

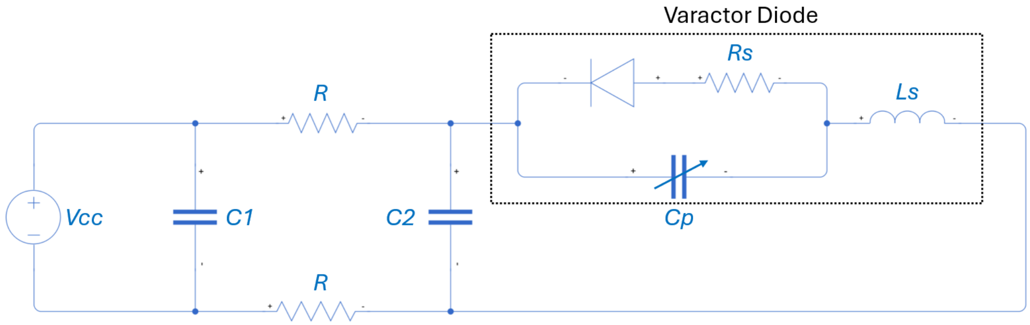

Figure 4.1: DC biasing circuit

The varactor diode operates under reverse bias, meaning that the positive terminal of the DC supply must be connected to the cathode of the diode, while the nominal values of the elements in its equivalent circuit are taken from the manufacturer's datasheet.

A parallel capacitor $C1$ = 82 pF maintains the bias source at RF ground, this contributes to isolating the resonator from noise or leakage through the DC supply.

Each resistor R provides a path between the source and the varactor diode, its value has been chosen large enough (R = 10 kΩ) to ensure a high impedance at RF. In steady-state operation, the reverse-biased varactor draws negligible DC current, resulting in a minimal voltage drop across these resistors.

Finally, a bypass capacitor $C2$ = 33 pF is included to allow the application of a DC voltage across the varactor while preserving the RF behavior of the resonator. Since its terminals are connected across a small gap in one arm of the resonator, this path behaves approximately as a short circuit at RF, whereas for DC it remains an open circuit. Therefore, the bias network provides the required tuning voltage while maintaining proper RF isolation.

The components chosen for this work are detailed in Table. 4.1.

Table 4.1: Components used for the DC biasing circuit

Type of component	Model	Value
Varactor diode	SMV1247 SC-79	0.64 - 8.86 pF
Chip resistor	SMD 0805	10 kΩ
Capacitor	S603DS	33 pF, 82 pF

The DC biasing circuit was first implemented in the single-resonator configuration in order to compare the measured behavior with the simulation results. This initial validation provides a basis for evaluating the effectiveness of the tunable filter and the integration of the DC biasing circuit. The implementation and corresponding results are presented in the following section.

4.2 Fabrication of a Single Resonator

The single resonator, which constitutes the fundamental building block of the proposed filter, was fabricated and measured in order to compare its frequency response with the simulated results. To enable tuning, the DC biasing circuit introduced in the previous section was integrated into the single-resonator layout. This step is important because it allows the practical implementation of the varactor-based tuning mechanism while also providing an initial validation of the biasing approach before extending it to the complete filter structure.

As discussed previously, the bypass capacitor is connected across a small cut introduced in one arm of the resonator. However, the location of this cut must be selected carefully to minimize its impact on the RF behavior of the resonator. For this reason, an electromagnetic field analysis was carried out prior to fabrication. In particular, the electric field distribution and the surface current density were examined to identify a suitable region for the small cut.

The preferred location, as illustrated in Fig. 4.2, is a region where the electric field magnitude is relatively low and there is not a high current concentration. As a result, the discontinuity in that area is less likely to perturb the resonant response or modify the coupling behavior. This indicator also provides a useful design reference for introducing similar cuts in the fourth-order bandstop filter presented later in this work.

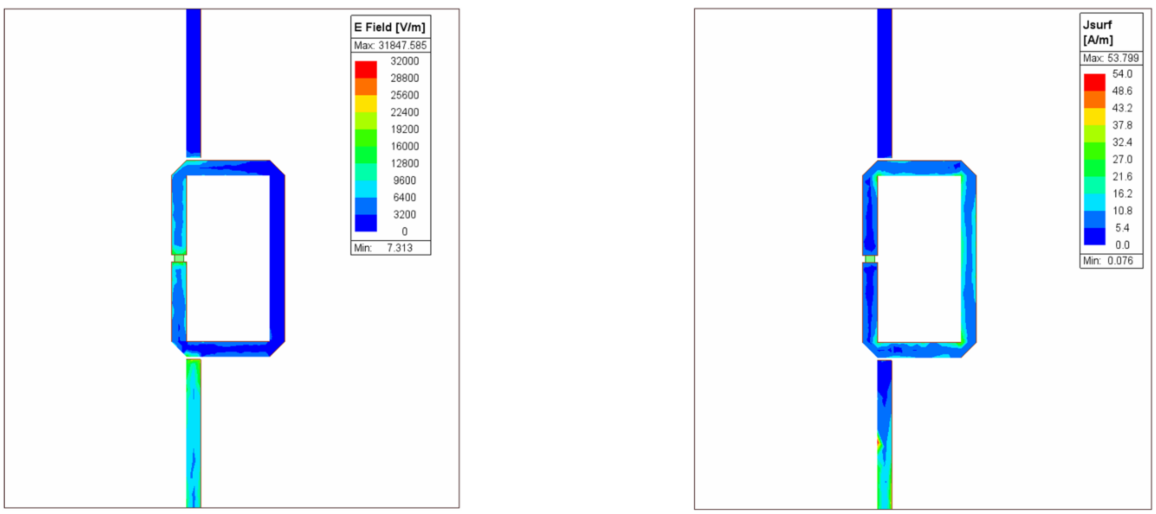

(a) (b)

Figure 4.2: a) Electric field distribution, b) Surface current density.

The fabricated single-resonator is shown in Fig. 4.3. Before fabrication, the full-wave EM simulation was performed to the layout including the DC biasing circuit to account for the integration of its components and verify that the frequency response has not been perturbed.

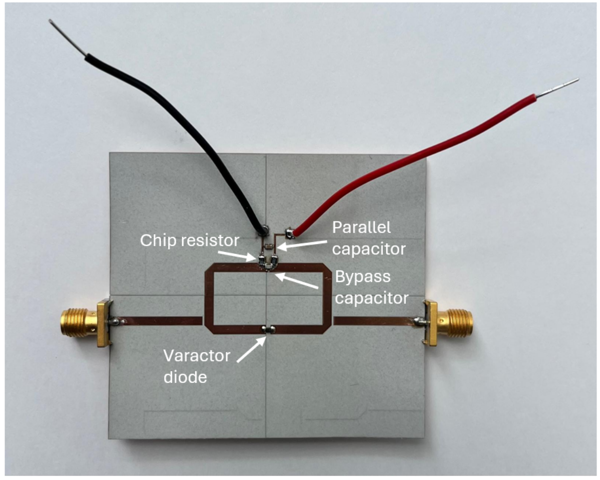

Figure 4.3: Fabricated single resonator

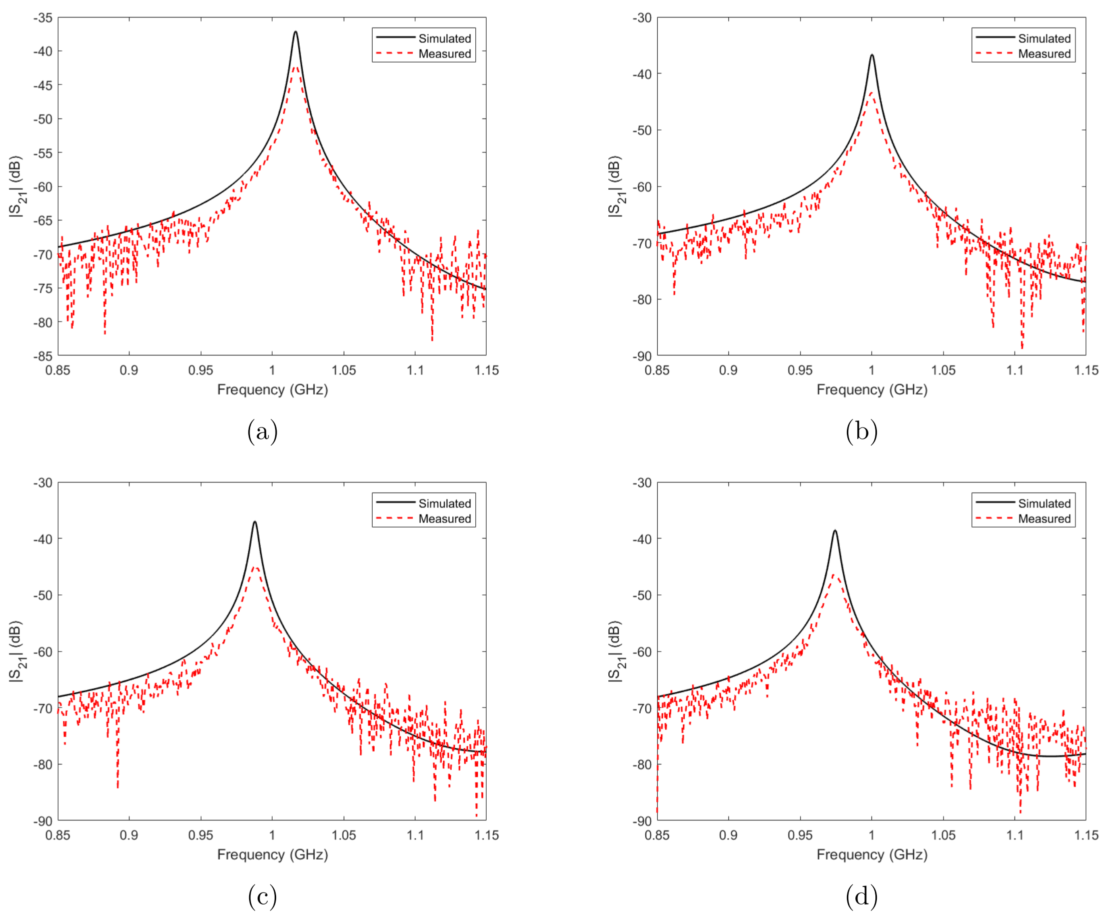

Figure 4.4: Comparison between simulated and measured values for a single resonator with an ideal varactor: a) At 0.68 pF, b) At 0.71 pF, c) At 0.76 pF, d) At 0.83 pF

The measured response shown in Fig. 4.4 exhibits a transmission peak approximately 8 dB lower than that simulated response. This discrepancy can be attributed to practical non-ideal behavior of the varactor, which will be analyzed closely in the next section.

Among other contributing factors are the actual dielectric constant of the substrate relative to the value assumed in simulation, soldering effects, connector losses, and other parasitic elements that are not fully captured in the ideal model.

The measured tuning range of the single resonator extends from 0.64 pF to 1.22 pF, corresponding to an approximate frequency shift of 223 MHz around a 1 GHz center frequency, as illustrated in Fig. 4.5. This usable tuning range is limited by the loading characteristics of the selected resonator structure.

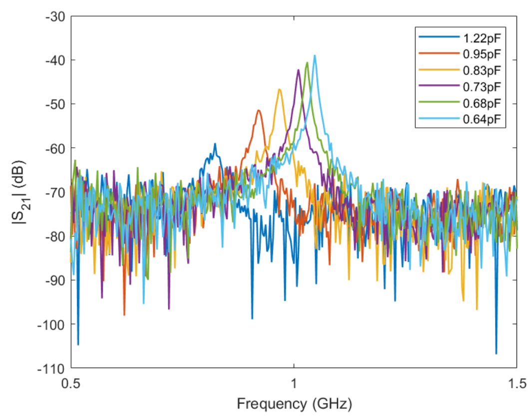

Figure 4.5: Single resonator tuning range

Although the datasheet of the chosen varactor specifies capacitance values up to 8.86 pF, the full nominal range is not practically usable in this implementation. This behavior is observed when the DC bias voltage is reduced below 2.5 V, which corresponds to approximately 1.22 pF, the measured frequency response becomes nearly flat with an amplitude comparable to that observed in the rejection region. Under these conditions, the resonance is no longer clearly distinguishable.

This behavior indicates that, once the varactor diode is integrated between the arms of the resonator, the resulting structure no longer behaves as an isolated component with variable capacitance. Instead, the usable capacitance range becomes strongly influenced by the interaction between the varactor and the fringing fields across the arms of the resonator, like an effective combined capacitive loading. As a result, the relationship between the applied bias voltage and the resonant frequency is not determined only by the nominal capacitance values provided in the datasheet, but also by the electromagnetic interaction within the physical structure.

Furthermore, the measured response indicates a lower unloaded quality factor than that predicted by the ideal model. This reduction is expected because the fabricated resonator includes additional loss mechanisms that are not fully represented in the ideal simulation. In general, the unloaded quality factor of a microstrip resonator can be expressed in terms of the dielectric, conductor, and radiation loss contributions, represented by Q_d, Q_c, and Q_r in the expression below [9].

$$\frac{1}{Q_u} = \frac{1}{Q_d} + \frac{1}{Q_c} + \frac{1}{Q_r} \tag{4.1}$$

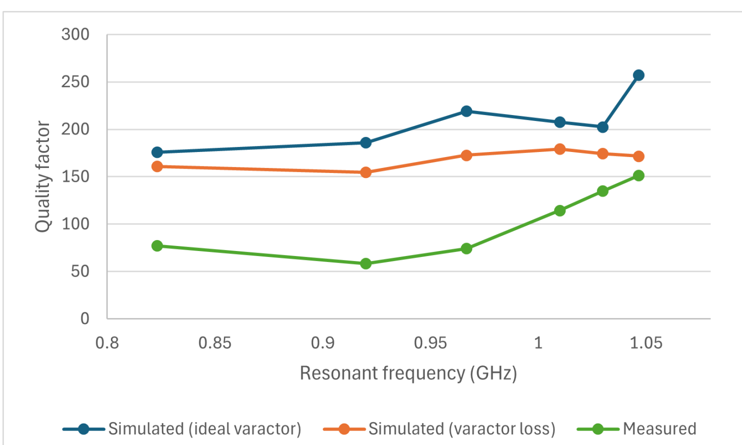

Figure 4.6: Measured and simulated quality factor of the microstrip single resonator. Adapted from [15]

In addition to the intrinsic losses of the microstrip resonator, the varactor diode introduces an additional loss. Therefore, when the tuning element is included, the total unloaded quality factor can be approximated by separating the resonator contribution from the varactor contribution. This relationship follows the same form used in the previous expression, where independent loss mechanisms add through their reciprocal quality factors, as shown in (4.2).

$$\frac{1}{Q_u} = \frac{1}{Q_{res}} + \frac{1}{Q_{var}} \tag{4.2}$$

In this expression, Q_{res} represents the quality factor associated with the resonator when the varactor is modeled as an ideal tuning capacitance, while Q_{var} represents the additional loss introduced by the series resistance of the diode. Using the measured and simulated unloaded quality factors, along with the nominal capacitance value and the resonant frequency, the equivalent series resistance of the varactor was estimated. This calculation resulted in $R_s = 2.4\ \Omega$, which is close to the nominal value provided in the datasheet.

After extracting this equivalent series resistance, the varactor was no longer modeled as an ideal tuning capacitance. Instead, its loss contribution was included in the full-wave simulation. As shown in Fig. 4.7, the simulation including the varactor losses exhibits better agreement with the measured response than the simulation based on an ideal varactor. This confirms that the quality factor of the tuning element contributes noticeably to the reduction in the resonator peak amplitude.

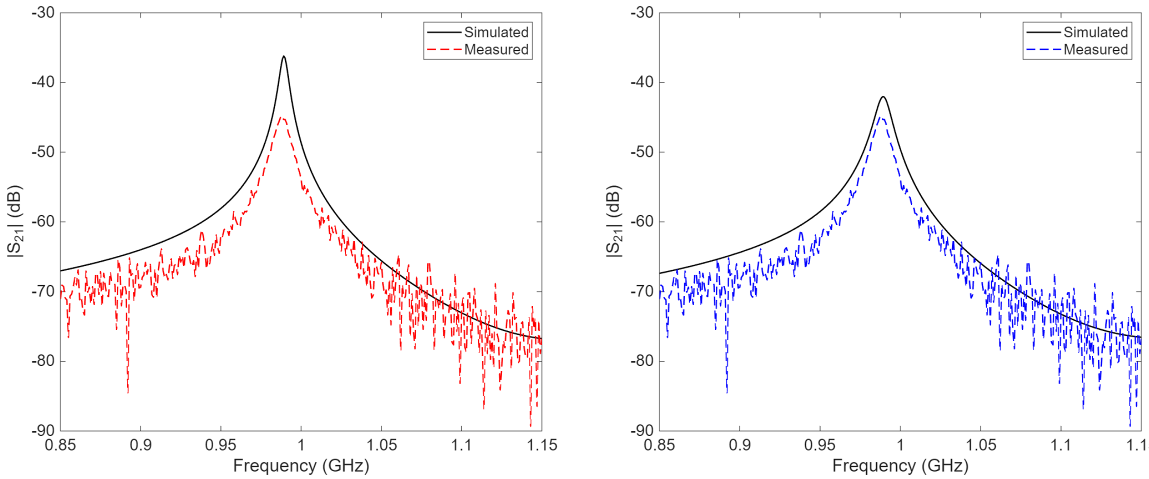

(a) (b)

Figure 4.7: Comparison between simulated and measured single-resonator responses: a) lossless varactor, b) including the estimated varactor loss

As observed before, the estimated varactor-loss model provides a closer representation of the measured response, particularly in terms of the peak transmission level near resonance. While a difference between simulation and measurement is still present, the reduced discrepancy confirms that the varactor series resistance is an important loss mechanism in the fabricated resonator. The remaining mismatch can be attributed to parasitic effects not fully captured in the model, such as soldering, connector transitions, and substrate tolerances.

Overall, the single-resonator analysis provides an essential starting point for the development of the complete tunable bandstop filter, since it allows the resonant behavior, tuning capability, and biasing implementation to be validated in an isolated and controlled configuration. The measured results are in good agreement with the expected response, confirming the tunable nature of the resonator and demonstrating that the proposed DC biasing circuit operates correctly in practice. Therefore, this preliminary validation establishes a reliable foundation for the implementation and analysis of the higher-order tunable filter presented in this chapter.

4.3 Bandstop Filter Considerations

Throughout this work, a Chebyshev fourth-order bandstop filter has been synthesized, designed, and simulated using full-wave EM software tools. However, before proceeding with the fabrication, some practical considerations must be addressed.

The first one is the length of the tapped line, which was increased to obtain a response that closely matches the phase behavior of the ideal filter. This adjustment is related to the operating principle of the bandstop filter, where the overall response is determined by the interaction between the direct source-to-load path and the resonant path through the coupled resonators. For the desired bandstop response to be achieved, the relative phase of these two contributions must be aligned. This effect is illustrated in Fig. 4.8.

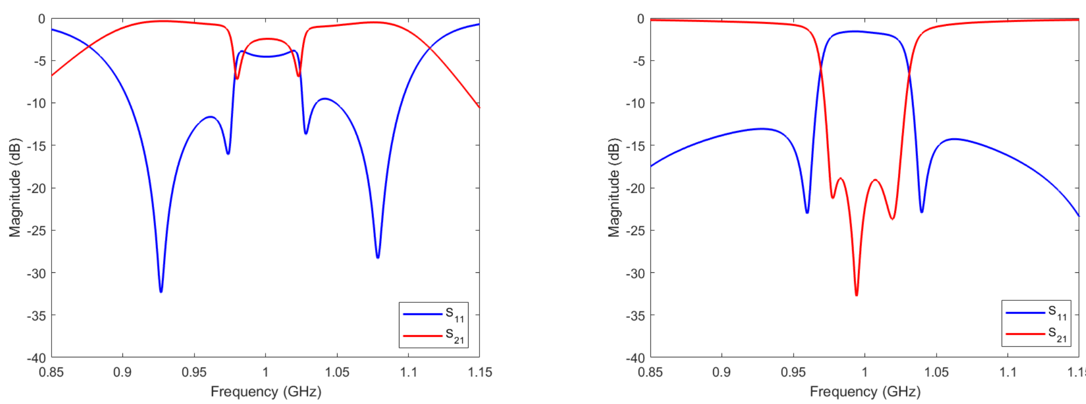

(a) (b)

Figure 4.8: Bandstop filter a) with original tapped-line length, b) after increasing tapped-line length

As shown in Fig. 4.8(a), the original tapped-line length does not provide the appropriate phase condition, which leads to a distorted stopband response and misalignment in both transmission and reflection characteristics. After increasing the tapped-line length, as observed in Fig. 4.8(b), the rejection becomes better defined at the desired frequency. This behavior can be attributed to the additional electrical length introduced by the tapped line, which improves the phase condition required to generate the stopband while simultaneously modifying the external coupling of the resonator.

The second consideration is the implementation of the direct source-to-load coupling term, represented in the coupling matrix as $M_{SL} = M_{LS} = 1$. In the microstrip realization, this coupling was implemented by a 50 Ω transmission line with an electrical length of 90°. The corresponding physical dimensions were initially determined using Microwave Office as the full-wave EM design software. In the final layout, these dimensions were further adjusted so that the required electrical length could be distributed along the direct path between the input and output ports. The resulting dimensions were $L = 42.252$ mm, and $W = 1.89061$ mm.

Additionally, as observed in the frequency response, the two transmission zeros are distinguishable, however, the stopband does not exhibit the same equi-ripple predicted by the inverted-based model. This deviation is associated with a slight shift in the resonant behavior between R1 and R2, as well as between R3 and R4, as illustrated in Fig. 4.9(c). The shift is inherently related to the physical resonator arrangement. Once the couplings k_{14} and k_{23} are adjusted, the position of the four resonators becomes fixed. Under these conditions, the coupling $k_{12} = k_{34}$ must be found without altering the position of the four resonators, even when the extracted S_{21} response is not perfectly centered at the resonant frequency.

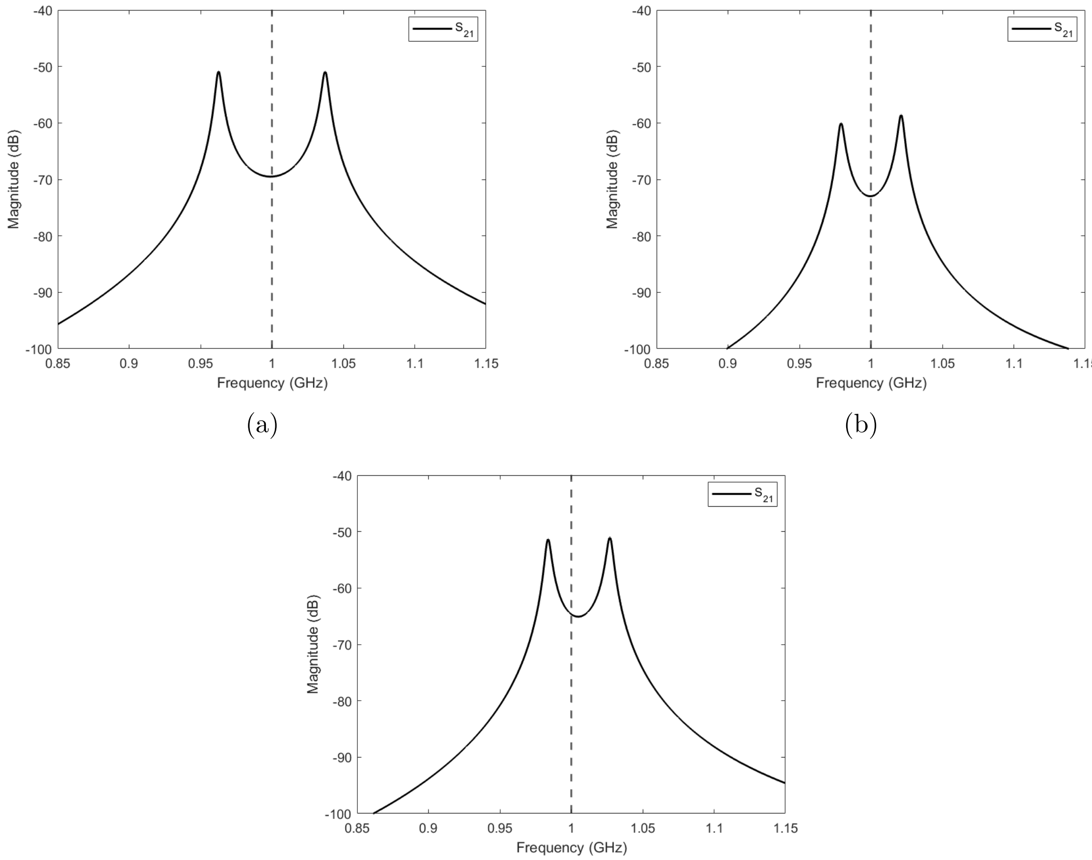

(a)

(b)

(c)

Figure 4.9: Inter-resonator coupling a) k_{14}, b) k_{23}, c) $k_{12} = k_{34}$

Finally, the small mismatch observed in the time-domain response after fine-tuning can be attributed to the location-dependent behavior of the physical resonators. Whereas each coupling coefficient is initially extracted from simplified resonator configurations, the couplings in the complete microstrip layout are not entirely independent. In the full structure, the response of each resonator is influenced not only by adjacent coupling, but also by cross-coupling effects. As a result, a perfect agreement with the ideal time-domain response was not achieved in the full-wave implementation.

In the next section, the final layout of the bandstop filter is presented, along with the measured results and their comparison with the simulated response.

4.4 Final Bandstop Filter Layout

The final microstrip layout of the tunable bandstop filter is shown in Fig. 4.10, along with its corresponding physical dimensions. This structure represents the final implementation obtained after the synthesis procedure, full-wave electromagnetic simulation, and fine-tuning through the time-domain tuning technique described in the previous chapter.

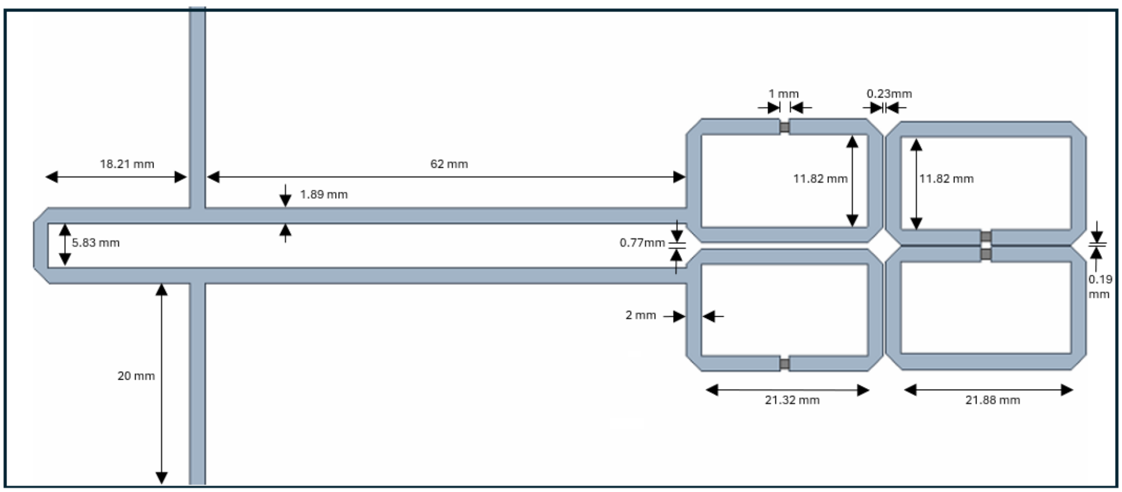

Figure 4.10: Final bandstop dimensions

One of the main advantages of microstrip technology is its relatively compact and planar implementation, which makes it suitable for practical microwave filter realization. Despite incorporation of four resonators, the feeding structure, and the DC-biasing network, the final prototype remains relatively compact when compared with other microwave filter technologies. The overall dimensions of the implemented filter are $0.34\lambda_g \times 0.85\lambda_g$, which is comparable to bandstop designs reported in [24, 25, 26].

The simulated tuning behavior of the final bandstop filter is presented in Fig. 4.11. As observed, the center frequency can be shifted from 965 MHz to 1.048 GHz while maintaining a stopband rejection of at least 10 dB. Therefore, only a portion of the nominal tuning range can be effectively used while preserving an acceptable bandstop response.

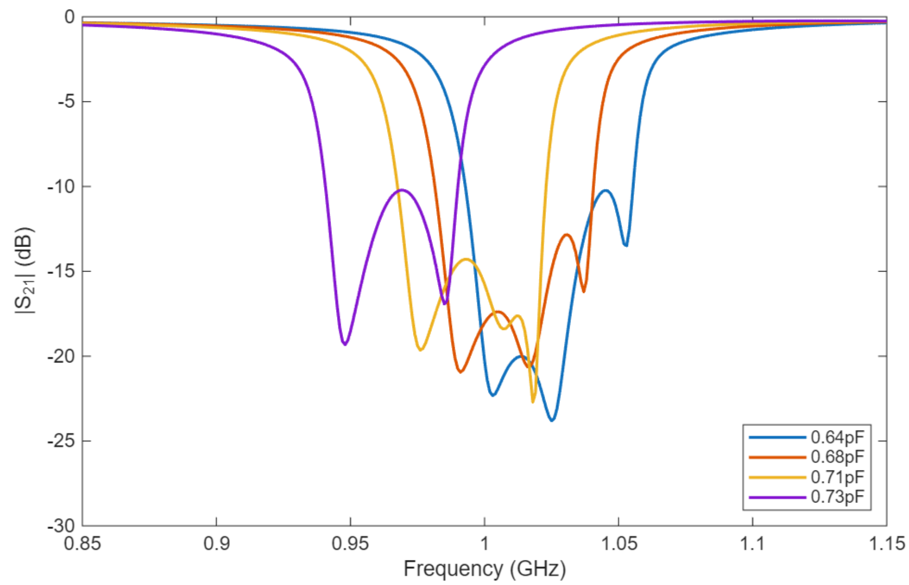

Figure 4.11: Bandstop S_{21} for different capacitance values

Despite the fact that this result confirms the tunability characteristic, the achievable tuning range of the complete bandstop filter is more limited than the one obtained for the single resonator. This reduction is expected, since in the full filter configuration each resonator is no longer affected only by its own loaded capacitance, but also by the electromagnetic interaction with adjacent resonators, external loading, and coupling within the network. As a result, the effective tuning contribution of each varactor is constrained by the collective behavior of the structure rather than by the isolated resonator alone.

The physical realization of the proposed design is presented in the next section, where the fabricated bandstop filter prototype is shown and its measured performance is discussed in comparison with the simulated results.

4.5 Fabrication and Experimental Results of the Bandstop Prototype

The fabricated fourth-order bandstop filter is shown in Fig. 4.12. This prototype corresponds to the final microstrip implementation of the proposed tunable filter, including the resonators, feeding network, and integrated DC-biasing circuit required for varactor tuning.

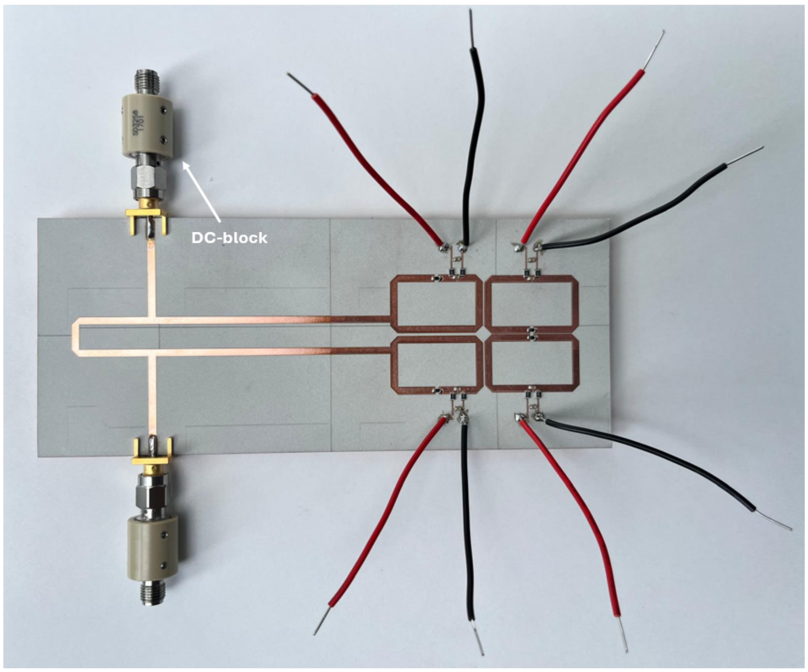

Figure 4.12: Fabricated 4x2 bandstop filter

The fabrication process introduced several practical challenges, mainly due to the integration of small components and multiple DC connections within a compact layout. In this type of implementation, careful soldering is essential to avoid unintended parasitic effects and to preserve mechanical reliability. Similarly, the contact pads used for the DC-biasing wires must provide sufficient area to ensure proper electrical contact and stable handling during measurement.

Additionally, as illustrated in Fig. 4.12, a DC-block was used between the fabricated filter and the RF network analyzer. This precaution was adopted to prevent DC current from reaching the measurement equipment and to protect the network analyzer during the realization of the DC biasing circuit.

The voltage measured across the varactor diodes remained very close to the applied bias voltage. This behavior is expected because the DC current flowing through the biasing network is extremely small, on the order of a few nanoamperes, resulting in a negligible voltage drop across the chip resistors. Therefore, the applied voltage can be considered a good approximation of the actual reverse voltage across the varactors.

The measured reverse-voltage values, along with the corresponding center frequency, bandwidth, and range of capacitance values are summarized in Table 4.2. As the reverse voltage increases from 3.1 V to 5.7 V, the center frequency shifts from 945 MHz to 1.048 GHz, confirming the expected varactor-controlled tuning capability of the prototype. In general, higher reverse-bias voltages correspond to lower effective capacitance values, which increases the resonant frequency of the structure. The table also shows that the fractional bandwidth is not constant throughout the tuning range. This indicates that the tuning process affects not only the center frequency, but also the coupling conditions within the filter, leading to changes in bandwidth as the capacitance is varied.

Table 4.2: Applied Reverse-Bias Voltage and Filter Tuning Parameters

Reverse Voltage (V)	f_c (MHz)	FBW	Range of capacitance (pF)
3.1	945	3.83%	0.83 - 0.95
3.2	950	3.74%	0.83 - 0.95
3.3	960	3.70%	0.83 - 0.95
3.4	970	3.68%	0.83 - 0.95
3.5	980	3.66%	0.83 - 0.95
3.7	990	3.39%	0.77 - 0.83
4.0	1,000	4.91%	0.77
4.7	1,030	5.10%	0.70 - 0.73
5.7	1,048	5.18%	0.67 - 0.68

The measured responses in Fig. 4.13 confirm that the fabricated bandstop filter preserves its tunable behavior, as a clear shift in the resonant frequency is observed when the reverse-bias voltage is varied. This verifies the functionality of the integrated DC-biasing circuit and confirms that the varactors effectively control the resonant frequency of the filter.

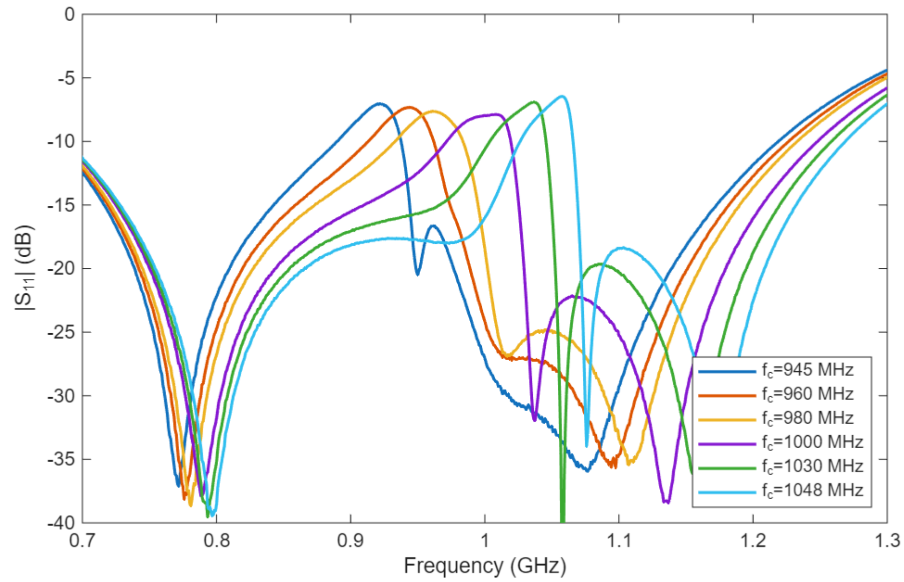

(a)

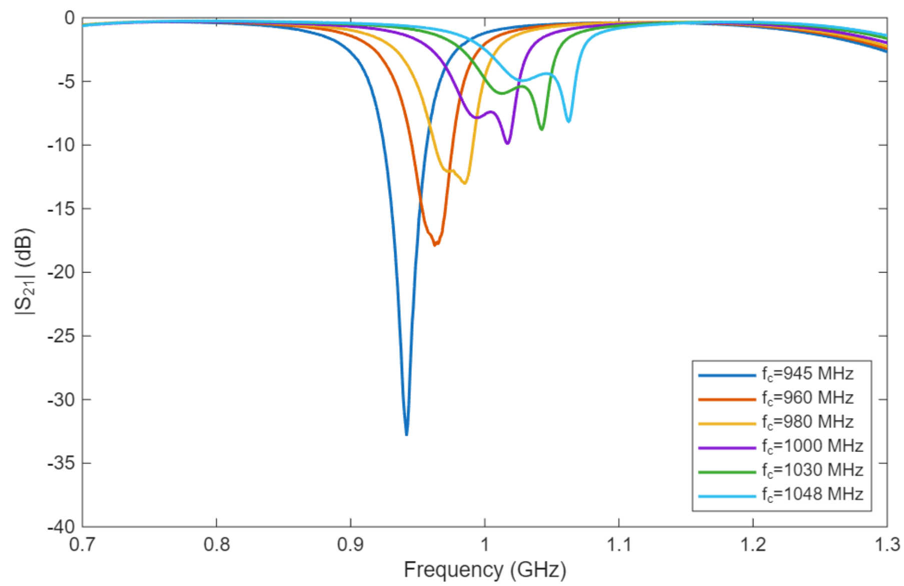

(b)

Figure 4.13: Measured tunable frequency response of the fabricated bandstop filter a) S_{11}, b) S_{21}.

Although the measured results demonstrate the intended tuning behavior, the response also exhibits practical limitations when compared with the simulated design.

In particular, the measured stopband shows a less uniform equi-ripple behavior, a more irregular out-of-band response, and additional spurious features that are not present in the ideal simulation. These discrepancies can be attributed to conductor and dielectric losses, soldering parasitics, connector transitions, varactor losses, fabrication tolerances, and additional effects introduced by the practical biasing network.

4.6 Frequency Response Analysis of the Bandstop Prototype

The frequency response of the bandstop prototype was analyzed by comparing the different stages of the design process, including the circuit-level model, the full-wave electromagnetic simulation, and the measured response of the fabricated filter. During this process, several practical factors were found to influence the final response. Among the most relevant, the tapped-line length required careful adjustment because it affected both the phase relationship between the scattering parameters and the interaction between the direct source-load path and the resonant path. In addition, the close spacing between resonators introduced parasitic couplings that modified the stopband behavior. These effects show that the transition from synthesis to physical implementation requires progressive refinement through simulation and experimental tuning..

This transition is illustrated in Fig. 4.14, where the response obtained in Microwave Office is compared with the corresponding Ansys HFSS result after tuning refinement. Both responses exhibit a bandstop characteristic centered near 1 GHz. However, the HFSS response shows a different stopband shape. In particular, the number and depth of the reflection zeros are not fully preserved between the two simulations. This difference is mainly associated with the additional physical effects captured in the EM model, including the influence of the biasing network.

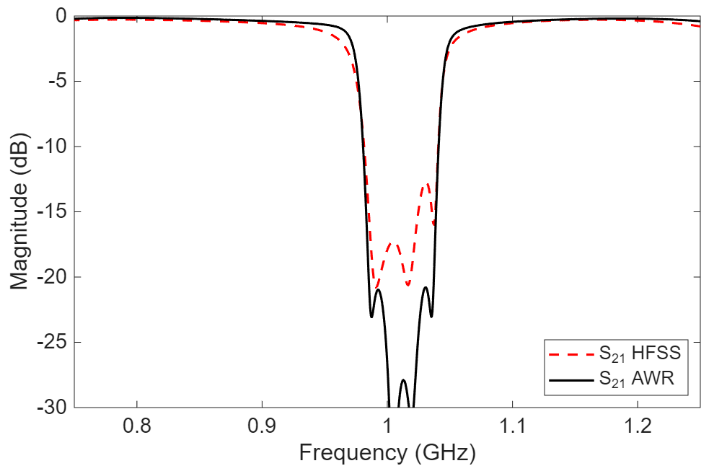

Figure 4.14: Comparison between the Microwave Office and Ansys HFSS simulated responses

A further comparison between the HFSS and measured responses is shown in Fig. 4.15. The fabricated prototype follows the general trend predicted by simulation, but differences remain in terms of stopband depth, ripple level and reflection-zero locations. The measured response presents a reduced rejection level and less pronounced ripple compared to the simulated response. These discrepancies are consistent with the effects of fabrication tolerances, connector and soldering parasitics, substrate parameter variations, varactor modeling, and additional losses introduced by the practical biasing circuit.

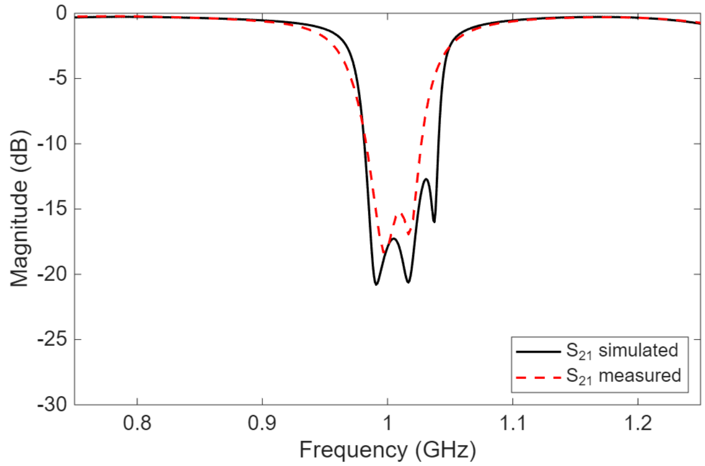

Figure 4.15: Comparison between the Ansys HFSS simulated response and the measured response

Despite the differences between the simulated and measured responses, the fabricated prototype provided experimental validation of the proposed concept. The results demonstrated that the characteristic-polynomial transformation can be translated into a practical microstrip implementation capable of producing a tunable bandstop response. In addition, the work included the development of a MATLAB script that automates the synthesis procedure by computing the transmission, reflection, and denominator polynomials, generating the corresponding transversal coupling matrices for both the original bandpass prototype and the transformed bandstop equivalent, and evaluating the normalized frequency response.

Overall, the planar prototype validated the theoretical bandpass-to-bandstop transformation and demonstrated the realization of a tunable bandstop filter with a wider rejection response than that typically obtained from a notch filter. This objective was achieved through a complete design process that included synthesis, full-wave simulation, experimental fabrication, and testing.

Chapter 5

Conclusion and Future Work

5.1 Conclusion

The advancements in microwave filter technologies require an special attention in developing bandstop filters to suppress unwanted signals over wider rejection bandwidths. In this work, an alternative synthesis approach was investigated by interchanging the transmission and reflection numerators of the characteristic polynomials of a bandpass prototype to obtain an equivalent bandstop response. This transformation established the theoretical foundation of the proposed design and provided a direct connection between the analytical response, the coupling-matrix formulation, and the physical implementation of the filter.

The results confirmed that the proposed characteristic-polynomial transformation is a valid and effective approach for generating a wider bandstop response. This was demonstrated through the complete design, simulation, fabrication, and measurement of a tunable microstrip bandstop filter prototype. The measured results successfully exhibited the main filtering characteristics predicted by the synthesis method and verified the practical feasibility of translating the theoretical transformation into a physical microstrip implementation.

In addition to the experimental validation, a MATLAB script was developed to automate the characteristic-polynomial synthesis procedure. The script provides sufficient flexibility to support different filter orders and response types, including symmetric, asymmetric, and fully canonical responses. Therefore, its use is not limited to the fourth-order prototype demonstrated in this work, but can also be extended to other filtering functions within the same synthesis framework.

In summary, this work established a complete framework for the design of a tunable microstrip bandstop filter, from characteristic-polynomial synthesis and coupling-matrix formulation to simulation, fabrication, and experimental validation. The results demonstrated that interchanging the characteristic-polynomial numerators provides an effective method for obtaining a wider bandstop response from a bandpass prototype, confirming the feasibility and practical value of the proposed synthesis approach.

5.2 Future Work

The proposed design may be extended by investigating alternative resonator topologies that provide greater flexibility in controlling not only the center frequency, but also the bandwidth and shape of the rejection response. In addition, the use of lower-loss structures and tuning components could help reduce the discrepancies observed among the synthesized, simulated, and measured responses. This improvement could be further supported by incorporating lossy synthesis into the design stage, allowing the losses associated with practical tuning elements, such as varactor diodes, to be considered in the full-wave simulation. By accounting for these non-ideal effects earlier in the synthesis process, the predicted response may more closely represent the fabricated prototype, particularly in terms of rejection level, insertion loss, and unloaded quality factor.

Although planar structures provide a practical and accessible platform for the implementation and experimental validation of advanced filtering techniques, alternative technologies may offer significant performance advantages for future developments, particularly in applications that require higher unloaded quality factor, lower loss, and improved power-handling capability, such as substrate-integrated evanescent-mode filters [27]. For this reason, even though the present work focused on a planar microstrip realization, the proposed synthesis methodology is not restricted to this specific filter technology.

The methodology presented in this work can also be extended to other tuning mechanisms that may provide a wider tuning range and improved control of the filter characteristics, such as RF MEMS [28] and Barium Strontium Titanate [29]. In this sense, this work establishes a structured framework for analyzing and translating fundamental filtering-function properties into a practical design methodology that can be adapted to other prototypes and implementation technologies.

Finally, the analysis presented in this work may also serve as a foundation for the development of higher-order filter structures and wide-passband bandstop filters [30]. By extending the concepts established here from the fourth-order case to more general configurations, it becomes possible to investigate more complex filtering responses with enhanced selectivity and additional transmission zeros. In this way, the mathematical and physical insights developed throughout this work can support future efforts toward the realization of more advanced filtering structures, with this work intended to serve as a foundation for future implementations based on the synthesis methodology presented, as illustrated in Fig. 5.1.

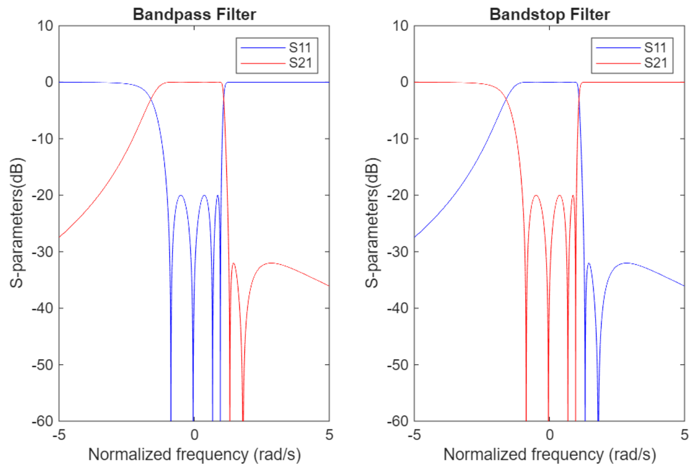

(a)

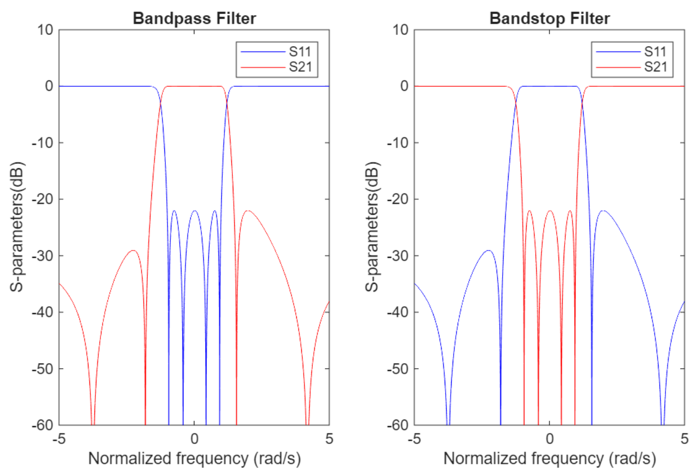

(b)

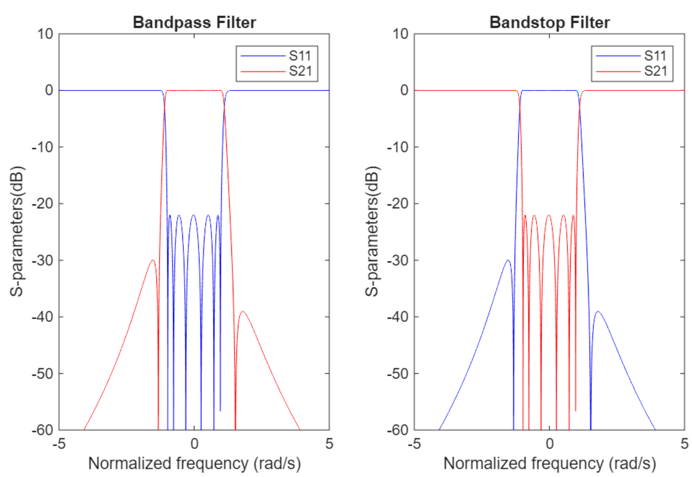

(c)

Figure 5.1: Multiple filters created using the MATLAB script developed in this work a) 4x2 asymmetric, b) 4x4 fully canonical, c) 6x2 asymmetric.

Appendix A

Appendix

A.1 Recursive Technique in MATLAB

The recursive algorithm used for the synthesis of the coupling matrix is shown in Listing A.1.

Listing A.1: Recursive technique

```
function [U, V] = recursiveUV(TZ)
% recursiveUV(TZ): Compute polynomial coefficients U, V for given
% transmission zeros
%   [U, V] = recursiveUV(TZ)
%
%   Input:
%     TZ : vector of prescribed TZ of length N
%   Output:
%     U, V : row-vectors of length N+1 containing the real and imaginary
%            parts of the recursive polynomial coefficients.
N = numel(TZ);
% Pre-allocate U and V to have a length of N+1 coefficients
U = zeros(1, N+1);
V = zeros(1, N+1);
```

```
% Initialize with first prescribed zero w1 = TZ(1)
X = 1/TZ(1);
Y = sqrt(1-X^2);
% Follow the polynomial structure G1(w) = U1(w) + V1(w)
U(1) = -X;
U(2) =  1;
V(1) =  Y;
V(2) =  0;
% Recursively multiply in the remaining zeros w2 to wN
for K = 3:N+1
    X = 1/TZ(K-1);
    Y = sqrt(1-X^2);
    % Pre-allocate the corresponding coefficients for each stage
    U2 = zeros(1,K);
    V2 = zeros(1,K);
    % Multiply by the constant term of (w - w_{K-1})
    for J = 1:K-1
        U2(J) = -U(J)*X-Y*V(J);
        V2(J) =-V(J)*X+Y*U(J);
    end
    % Multiply by the w term
    for J = 2:K
        U2(J) = U2(J) + U(J-1);
        V2(J) = V2(J) + V(J-1);
    end
    % Multiply by the w^2 term
    for J = 3:K
        U2(J) = U2(J) + Y*V(J-2);
    end
    % Copy back into U,V for next iteration
    U(1:K) = U2;
```

```
    V(1:K) = V2;
end
end
```

A.2 Bandpass-to-Bandstop Transformation in MATLAB

The bandpass-to-bandstop transformation is shown in Listing A.2.

Listing A.2: Bandpass-to-Banstop Transformation

```
% Returns characteristic polynomials P(s), F(s), E(s); the transversal
% coupling matrix for a bandpass and bandstop filter; and the corresponding
% graphic representation
% Inputs:
% n = filter order (for instance: 4)
% nfz = number of finite transmission zeros (for instance: 2)
% RL = magnitude of the return loss in dB (for instance: 22)
% TZ = location of all transmission zeros (w1,w2,...,wn) including those
% at infinity, between brackets and separated by comma.
% (for instance: [-1.5699, 1.5699, Inf, Inf])

n = input('Enter filter order: \n');
nfz = input('Enter number of finite transmission zeros: \n');
RL = input('Enter return loss in dB: \n');
TZ = input('Location of all TZ including those at infinity: \n');

% Determine vectors U and V using recursive method function
[U, V] = recursiveUV(TZ);
% Find the roots of U and V
```

```
U0 = flip(U);
U0_root = roots(U0);
V0 = flip(V);
V0_root = roots(V0);
% Calculate P(s)
P = 1; % Initialize the polynomial
for k = 1:length(TZ)
    if ~isinf(TZ(k))
        factor1 = [1, -1i*TZ(k)];
        P = conv(P, factor1);
    end
end
% Orthogonality property for (N - nfz) must be satisfied
if mod(n - nfz, 2) == 0
    Po = 1i*P;
else
    Po = P;
end
Ps = [zeros(1,n+1-length(Po)), Po]
% Calculate F(s)
root_f = 1i*U0_root;
Fs = poly(root_f)
% Calculate ripple and normalization constant
syms s
Pnew = 1; % Initialize the numerator
for j = 1:length(TZ)
    if ~isinf(TZ(j))
        num = (s -1i*TZ(j));
        Pnew = expand(Pnew*num);
    end
end
```

```
Fnew = 1; % Initialize the denominator
for m = 1:length(root_f)
    den = (s -1i*U0_root(m));
    Fnew = expand(Fnew*den);
end
num1 = double(subs(Pnew,s,-1/1i));
den1 = double(subs(Fnew,s,-1/1i));
num2 = double(subs(Pnew,s, 1/1i));
den2 = double(subs(Fnew,s, 1/1i));
if n == nfz
    eps1= (1/sqrt(10^(RL/10) -1))*abs(num1)/abs(den1);
    er1 = eps1/(sqrt(eps1^2 -1));
    eps2= (1/sqrt(10^(RL/10) -1))*abs(num2)/abs(den2);
    er2 = eps2/(sqrt(eps2^2 -1));
else
    eps1 = (1/sqrt(10^(RL/10) -1))*abs(num1)/abs(den1);
    er1 = 1;
    eps2 = (1/sqrt(10^(RL/10) -1))*abs(num2)/abs(den2);
    er2 = 1;
end
if round(eps1,3) == round(eps2,3) % Must match up to three decimals
    eps = eps1; % Define one single value for epsilon and eR
    er = er1;
else
    disp('Compare epsilon values')
end
% Calculate E(s)
if mod(n - nfz, 2) == 0
    Pnew = 1i*Pnew;
else
    Pnew = 1*Pnew;
```

```
end
Es = (er*Pnew + eps*Fnew);
% Find the coefficients
coef = sym2poly(Es);
% Find the roots of E(s)
root_E = roots(coef);
% Take only the left side of the quadrant
n_e = length(root_E);
E = complex(zeros(1,n_e));
for x = 1:n_e
    if real(root_E(x)) < 0
        E(x) = real(root_E(x))+imag(root_E(x))*1i;
    else
        E(x) = -real(root_E(x))+imag(root_E(x))*1i;
    end
end
Es = poly(E)

% BANDPASS FILTER
Pbp = Ps/eps;
Fbp = Fs/er;
Eb = flip(Es);
Fb1 = flip(Fbp);
% Admittance polynomials
m1 = zeros(1,n+1);
n1 = zeros(1,n+1);
for d = 1:n+1
    if mod(d,2) == 1
        % odd index
        m1(d) = real(Eb(d))+real(Fb1(d));
        n1(d) = 1i*(imag(Eb(d))+imag(Fb1(d)));
```

```
    else
        % even index
        m1(d) = 1i*(imag(Eb(d))+imag(Fb1(d)));
        n1(d) = real(Eb(d))+real(Fb1(d));
    end
end
% Re-define the polynomials using the admittance equivalence
if mod(n,2) == 0
    y21np = Pbp;
    y22np = flip(n1);
    ydp = flip(m1);
else
    y21np = Pbp;
    y22np = flip(m1);
    ydp = flip(n1);
end
% Partial fraction expansion
[r21p p21p k21p] = residue(y21np,ydp);
[r22p p22p k22p] = residue(y22np,ydp);
% Sort the values in ascending order
im1 = imag(p21p);
[~, idx] = sort(im1);
p21p_sorted = p21p(idx);
r21p_sorted = r21p(idx);
im2 = imag(p22p);
[~, idx] = sort(im2);
p22p_sorted = p22p(idx);
r22p_sorted = r22p(idx);
% Eigen values
lam1 = imag(p21p_sorted);
r22kp = real(r22p_sorted);
```

```
r21kp = real(r21p_sorted);
for k = 1:n
    Sqp(k) = sqrt(r22kp(k));
    Dip(k) = r21kp(k)/Sqp(k);
end
if isempty(k21p)
    C1 = 0;
else
    C1 = imag(k21p);
end
% Coupling Matrix
Mbpf = zeros(n+2);
Mbpf(1,2:n+1) = Dip; % First column
Mbpf(2:n+1,1) = transpose(Dip); % First row
Mbpf(2:n+1,2:n+1) = -diag(lam1); % Diagonal of lambdas
Mbpf(n+2,2:n+1) = Sqp; % Last row
Mbpf(2:n+1,n+2) = transpose(Sqp); % Last column
Mbpf(1,n+2) = C1; % Direct source-load coupling
Mbpf(n+2,1) = C1; % Direct source-load coupling

% BANDSTOP FILTER
if mod(n - nfz, 2) == 0
    Pbsf = 1i*Fs;
    Fbsf = -1i*Ps;
else
    Pbsf = 1i*Fs;
    Fbsf = Ps;
end
Pbs = Pbsf/er;
Fbs = Fbsf/eps;
Fb2 = flip(Fbs);
```

```
% Admittance polynomials
m2 = zeros(1,n+1);
n2 = zeros(1,n+1);
for f = 1:n+1
    if mod(f,2) == 1
        % odd index
        m2(f) = real(Eb(f))+real(Fb2(f));
        n2(f) = 1i*(imag(Eb(f))+imag(Fb2(f)));
    else
        % even index
        m2(f) = 1i*(imag(Eb(f))+imag(Fb2(f)));
        n2(f) = real(Eb(f))+real(Fb2(f));
    end
end
% Re-define the polynomials using the admittance equivalence
if mod(n,2) == 0
    y21ns = Pbs;
    y22ns = flip(n2);
    yds = flip(m2);
else
    y21ns = Pbs;
    y22ns = flip(m2);
    yds = flip(n2);
end
% Partial fraction expansion
[r21s p21s k21s] = residue(y21ns,yds);
[r22s p22s k22s] = residue(y22ns,yds);
% Sort the values in ascending order
im3 = imag(p21s);
[~, idx] = sort(im3);
p21s_sorted = p21s(idx);
```

```
r21s_sorted = r21s(idx);
im4 = imag(p22s);
[~, idx] = sort(im4);
p22s_sorted = p22s(idx);
r22s_sorted = r22s(idx);
% Eigen values
lam2 = imag(p21s_sorted);
r22ks = real(r22s_sorted);
r21ks = real(r21s_sorted);
for k = 1:n
    Sqs(k) = sqrt(r22ks(k));
    Dis(k) = r21ks(k)/Sqs(k);
end
if isempty(k21s)
    C2 = 0;
else
    C2 = imag(k21s);
end
% Coupling Matrix
Mbsf = zeros(n+2);
Mbsf(1,2:n+1) = Dis; % First column
Mbsf(2:n+1,1) = transpose(Dis); % First row
Mbsf(2:n+1,2:n+1) = -diag(lam2); % Diagonal of lambdas
Mbsf(n+2,2:n+1) = Sqs; % Last row
Mbsf(2:n+1,n+2) = transpose(Sqs); % Last column
Mbsf(1,n+2) = C2; % Direct source-load coupling
Mbsf(n+2,1) = C2; % Direct source-load coupling
% Define source and load vector
R = zeros(n+2,n+2);
R(1,1) = 1;
R(n+2,n+2) = 1;
```

```
% Define a range for angular frequency
wc = linspace(-8,8,10000);
% Find de S-parameters
for x = 1:length(wc)
    w = wc(x);
    J = zeros(n+2,n+2);
    J(2:n+1,2:n+1) = 1i*w*eye(n);
    A = R + J + 1i*Mbpf;
    B = R + J + 1i*Mbsf;
    An = inv(A);
    Bn = inv(B);
    % Use matrix An and Bn to calculate s-params
    s11bp = 1 - 2*An(1,1,:);
    s21bp = 2*An(n+2,1,:);
    s11bs = 1 - 2*Bn(1,1,:);
    s21bs = 2*Bn(n+2,1,:);
    % Calculate the magnitude in dB
    s11p(x) = 10*log10((abs(s11bp))^2);
    s21p(x) = 10*log10((abs(s21bp))^2);
    s11s(x) = 10*log10((abs(s11bs))^2);
    s21s(x) = 10*log10((abs(s21bs))^2);
end

figure
subplot(1,2,1)
plot(wc,s11p, '-b','LineWidth', 1.5)
hold on
plot(wc, s21p, '-r','LineWidth', 1.5)
hold off
xlim([-5 5])
ylim([-60 0])
```

```
xlabel('Normalized frequency (rad/s)')
ylabel('Magnitude (dB)')
title('Bandpass Filter')
legend('S11', 'S21',Location='northeast')
subplot(1, 2, 2)
plot(wc,s11s, '-b','LineWidth', 1.5)
hold on
plot(wc, s21s, '-r','LineWidth', 1.5)
hold off
xlim([-5 5])
ylim([-60 0])
xlabel('Normalized frequency (rad/s)')
ylabel('Magnitude (dB)')
title('Bandstop Filter')
legend('S11', 'S21',Location='northeast')
```

References

[1] J.-S. Hong, "Reconfigurable planar filters," *IEEE Microwave Magazine*, vol. 10, no. 6, pp. 73–83, 2009.

[2] A. M. Zaidi, B. K. Kanaujia, J. Kishor, S. S. Singhwal, V. Kaim, A. Kumar, K. Rambabu, and S. R. Rengarajan, "Design techniques for passive planar reconfigurable RF circuits: Reconfigurable RF circuits," *IEEE Microwave Magazine*, vol. 25, no. 9, pp. 29–42, 2024.

[3] A. S. Saber, R. Moslemi, and D. Zarifi, "A Ku-band mechanically tunable bandstop filter in groove gap waveguide," *AEU-International Journal of Electronics and Communications*, p. 156153, 2025.

[4] Y.-H. Cho and G. M. Rebeiz, "0.7–1.0-GHz reconfigurable bandpass-to-bandstop filter with selectable 2- and 4-pole responses," *IEEE Transactions on Microwave Theory and Techniques*, vol. 62, no. 11, pp. 2626–2632, 2014.

[5] Y.-H. Cho and G. M. Rebeiz, "Two-and four-pole tunable 0.7-1.1-GHz bandpass-to-bandstop filters with bandwidth control," *IEEE Transactions on Microwave Theory and Techniques*, vol. 62, no. 3, pp. 457–463, 2014.

[6] Z. Sun, X. Wang, L. Zhu, G. Milinevsky, and G. Lu, "A novel ring type wideband quasi-elliptic bandstop filter with controllable equal ripple performance and extra-high attenuation rate," *IEEE Transactions on Microwave Theory and Techniques*, vol. 72, no. 7, pp. 4258–4268, 2024.

[7] S. Saeedi, J. Lee, and H. H. Sigmarsson, "Double conversion method for synthesis of inverse filters," in *2015 IEEE MTT-S International Microwave Symposium*, 2015, pp. 1–4.

[8] T. H. Lee, *Planar microwave engineering: a practical guide to theory, measurement, and circuits*. Cambridge university press, 2004, vol. 1.

[9] J.-S. G. Hong and M. J. Lancaster, *Microstrip filters for RF/microwave applications*. John Wiley & Sons, 2004.

[10] R. J. Cameron, C. M. Kudsia, and R. R. Mansour, *Microwave filters for communication systems: fundamentals, design, and applications*. John Wiley & Sons, 2018.

[11] R. J. Cameron, Y. Wang, and M. Yu, "Direct-coupled realizations for microwave bandstop filters," in *IEEE MTT-S International Microwave Symposium Digest, 2005.*, 2005, pp. 111–114.

[12] A. Atia and A. Williams, “New types of waveguide bandpass filters for satellite transponders,” *Comsat Tech. Review*, vol. 1, no. 1, pp. 20–43, 1971.

[13] J. S. Lee, *Microwave resonator filters for advanced wireless systems.* University of Michigan, 2009.

[14] S. Saeedi, J. Lee, and H. H. Sigmarsson, “Novel coupling matrix synthesis for single-layer substrate-integrated evanescent-mode cavity tunable bandstop filter design,” *IEEE Transactions on Microwave Theory and Techniques*, vol. 63, no. 12, pp. 3929–3938, 2015.

[15] A. Pham, “Reconfigurable filter design using liquid metal actuation,” 2021.

[16] A. Zakharov, S. Rozenko, and M. Ilchenko, “Varactor-tuned microstrip bandpass filter with loop hairpin and combline resonators,” *IEEE Transactions on Circuits and Systems II: Express Briefs*, vol. 66, no. 6, pp. 953–957, 2019.

[17] J.-S. Hong, H. Shaman, and Y.-H. Chun, “Dual-mode microstrip open-loop resonators and filters,” *IEEE Transactions on Microwave Theory and Techniques*, vol. 55, no. 8, pp. 1764–1770, 2007.

[18] T. Yang and G. M. Rebeiz, “Bandpass-to-bandstop reconfigurable tunable filters with frequency and bandwidth controls,” *IEEE Transactions on Microwave Theory and Techniques*, vol. 65, no. 7, pp. 2288–2297, 2017.

[19] A. Ebrahimi, T. Baum, J. Scott, and K. Ghorbani, “Continuously tunable dual-mode bandstop filter,” *IEEE Microwave and Wireless Components Letters*, vol. 28, no. 5, pp. 419–421, 2018.

[20] J. Ness, “A unified approach to the design, measurement, and tuning of coupled-resonator filters,” *IEEE Transactions on Microwave Theory and Techniques*, vol. 46, no. 4, pp. 343–351, 1998.

[21] J.-S. Hong and M. Lancaster, “Couplings of microstrip square open-loop resonators for cross-coupled planar microwave filters,” *IEEE Transactions on Microwave Theory and Techniques*, vol. 44, no. 11, pp. 2099–2109, 1996.

[22] J. P. Dunsmore, “The time-domain response of coupled-resonator filters with applications to tuning,” Ph.D. dissertation, University of Leeds, 2004.

[23] M. Thibodeau, “Theory, design, and fabrication of frequency agile filtennas,” 2020.

[24] S.-W. Ren, L.-S. Wu, H.-L. Peng, and J.-F. Mao, “A new wideband elliptic bandstop filter with cross coupling,” *IEEE Microwave and Wireless Components Letters*, vol. 25, no. 10, pp. 639–641, 2015.

[25] M. Kong, Y. Wu, Z. Zhuang, and Y. Liu, “Wideband bandstop filter with extreme sharp skirt selectivity,” *IEEE Microwave and Wireless Components Letters*, vol. 28, no. 12, pp. 1104–1106, 2018.

[26] F.-C. Chen, R.-S. Li, J.-M. Qiu, and Q.-X. Chu, “Sharp-rejection wideband bandstop filter using stepped impedance resonators,” *IEEE Transactions on Components, Packaging and Manufacturing Technology*, vol. 7, no. 3, pp. 444–449, 2017.

[27] J. Lee, E. J. Naglich, and W. J. Chappell, "Frequency response control in frequency-tunable bandstop filters," *IEEE Microwave and Wireless Components Letters*, vol. 20, no. 12, pp. 669–671, 2010.

[28] G. M. Rebeiz, K. Entesari, I. C. Reines, S.-J. Park, M. A. El-Tanani, A. Grichener, and A. R. Brown, "Tuning in to RF MEMS," *IEEE microwave magazine*, vol. 10, no. 6, pp. 55–72, 2009.

[29] K. W. Wong, R. R. Mansour, and G. Weale, "Reconfigurable bandstop and bandpass filters with wideband balun using IPD technology for frequency agile applications," *IEEE Transactions on Components, Packaging and Manufacturing Technology*, vol. 7, no. 4, pp. 610–620, 2017.

[30] K. Lee, J. Lee, and J. Lee, "Wide-passband bandstop filters," *IEEE Microwave Magazine*, 2026.